


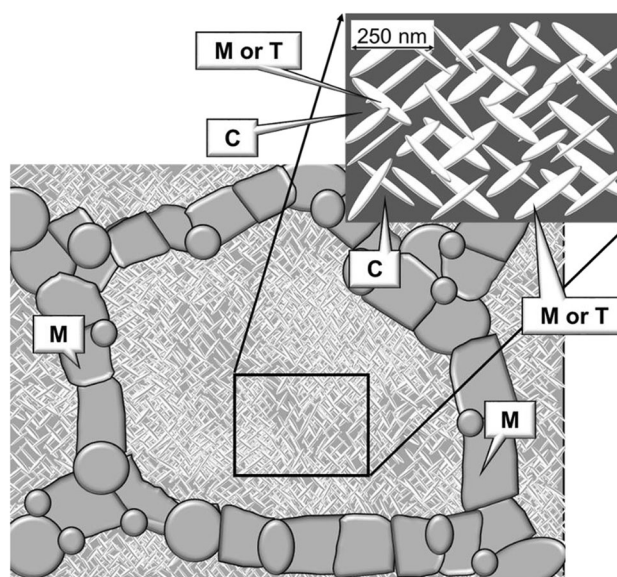
On the electrochemical properties of Mg-PSZ: an overview

A. I. B. Rondão¹ · E. N. S. Muccillo² · R. Muccillo² · F. M. B. Marques¹ 

Received: 23 April 2017 / Accepted: 8 August 2017 / Published online: 17 August 2017
© Springer Science+Business Media B.V. 2017

Abstract MgO-doped partially stabilized zirconia is a complex ceramic electrolyte in which all properties, phase composition, and microstructure are strongly influenced by thermal history besides chemical composition. The electrochemical performance of this ceramic used in oxygen sensors for molten steel is reviewed here. A wide collection of data on electrical properties obtained at various temperatures (up to 1600 °C) and oxygen partial pressures (from 1 atm to values below 10^{-20} atm) is considered. New aspects are brought to evidence after proper handling of published data on undoped zirconia and MgO-doped materials. The close temperature dependencies of the lower limits of the ionic domains of all these materials suggest the relevance of acceptor-type contaminations on the performance of nominally pure materials. High ionic mobility in the tetragonal phase with respect to the cubic phase is also likely, based on published data. Dopants like Y_2O_3 originate wider ionic domains but are not equally effective with respect to thermal shock resistance. The unique characteristics of MgO-doped zirconia are due to the coexistence of distinct phases, including large populations of finely dispersed monoclinic and/or tetragonal phases within cubic matrix grains. An overview of key features (materials and design) involved in the performance of oxygen sensors for molten steel is also provided.

Graphical abstract Typical microstructure of Mg-PSZ with multiple phases and interfaces



Keywords Mg-PSZ · Zirconia · Oxygen sensors · Ionic conductivity · Electronic conductivity

1 Introduction

Zirconia is among the best known ceramic materials due to an attractive range of properties. Tough zirconias are key engineering materials used in applications ranging from hot metal processing or heat-engines [1, 2] to pharmaceutical dies and dentistry [3–6]. Doping of zirconia is mandatory to extend the stability domain of the cubic (C) and/or tetragonal (T) phases. Proper compositional and microstructural tuning

✉ F. M. B. Marques
fmarques@ua.pt

¹ Department of Materials and Ceramic Engineering/CICECO, University of Aveiro, 3810-193 Aveiro, Portugal

² Center of Science and Technology of Materials, Energy and Nuclear Research Institute, São Paulo, SP 05508-900, Brazil

yields unrivaled performance in the so-called partially stabilized zirconias (PSZ), where the C and T phases prevail. The widely studied T to monoclinic (M) phase change has a main role on the thermomechanical performance [7–23], being the subject of several comprehensive reviews [24–26]. Relations between thermal history, microstructural development and performance are crucial [8, 11–14, 16, 18, 19, 23]. These materials develop in many aspects characteristics similar to those obtained with metal alloys when properly aged. Publications on PSZ are still active 50 years after the discovery of these materials [27].

Zirconia-based phase diagrams were under prolonged debate, with several versions available for most systems [28]. In binary systems including alkaline-earth oxides (e.g., MgO or CaO) or sesquioxides (e.g., Y_2O_3) there is a wide C phase field at high temperature for significant dopant levels [29–34]. In PSZ, the C and T phases may coexist at high temperature but are poorly stable at low temperature. The ZrO_2 –MgO system, central in this work, was extensively studied by distinct authors [29, 30, 35–41]. Problems in the determination of exact field boundaries due to slow equilibration, identification of new small fields (M + T [40]), and ordered phases like $Mg_2Zr_5O_{12}$ [16, 21, 37, 40] explain this situation. Anyhow, the most widely adopted diagrams indicate that the solubility of MgO either in the M or the T phases is quite limited (roughly 1–1.5 mol%). The exact eutectoid composition (C → T + MgO) is somewhat imprecise but within a narrow range of values (13–14.8 mol%) as well as the corresponding temperature (1400–1420 °C). The same is true for the T + MgO → M + MgO (or $Mg_2Zr_5O_{12}$) field transition (1120–1240 °C) [30, 40]. This means that phase diagrams can be clearly used as guidance. Here, the diagram suggested by Grain (Fig. 1) will be adopted as Ref. [30]. New information introduced throughout the years would imply only minor changes in the following discussion (e.g., see [36, 37, 40]).

PSZ is used namely in disposable Nernstian oxygen sensors for molten steel. Here excellent thermal shock resistance and large ionic domains are critical for a device reaching operating temperatures of 1600 °C and even higher within a few seconds. The thermomechanical characteristics surpass those often found in well-known materials like yttria-stabilized zirconia (YSZ). MgO-doped zirconia is the state of the art material used in this case and Mg-PSZ the corresponding acronym. The still growing number of patents on these materials and sensors illustrate the continuous interest on their performance [42–50]. Patents cover subjects ranging from sensor concept/design [42–46] to the processing route of Mg-PSZ [47–50].

Most of the underlying knowledge on the production of PSZ for oxygen sensors is patent protected, while significant information on the electrical properties of PSZ is

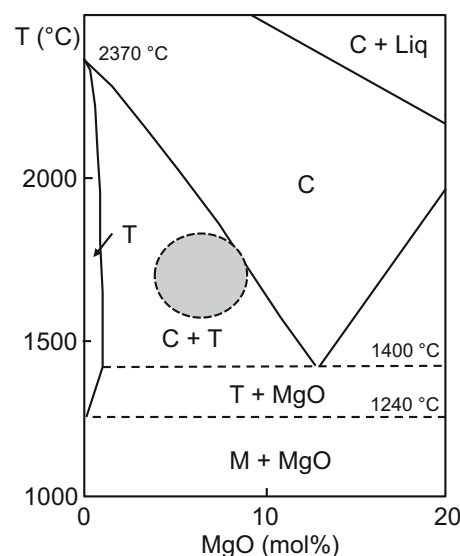


Fig. 1 Section of the ZrO_2 –MgO phase diagram where the shadowed area highlights a typical range of compositions and firing temperatures often used in the production of Mg-PSZ Adapted from [30]

disclosed but never duly gathered. A critical overview of these data will be presented here. Rather than a simple collection of data, emphasis will be on novel features not yet considered in these complex systems. Yet, background information must be firstly introduced.

In Mg-PSZ the T → M phase transition is martensitic, while the C → T transformation involves diffusion of Mg^{2+} cations [11, 13, 14, 17, 23]. Even so, for typical molten steel operating temperatures the system is believed to reach a condition close to thermodynamic equilibrium within a few seconds [51–53]. Thus, standard Mg-PSZ electrolytes are biphasic (C + T) materials at operating temperatures. For normal compositions (<10 mol% MgO) the C phase prevails but the role of the T phase should not be neglected. At temperatures below the eutectoid temperature (1400 °C), when a drift in the sensor signal is reported [54], the role of the T phase is certainly higher.

In zirconia-based electrolytes, oxygen vacancies are formed to compensate the charge of aliovalent dopants like Mg^{2+} or Y^{3+} . The higher the concentration of dopant, the higher the concentration of oxygen vacancies. Accordingly, the C phase, with higher dopant content, should possess higher ionic conductivity. However, the conductivity of the T phase (with lower dopant content) might surpass that of C zirconia. This is well-documented in the case of the ZrO_2 – Y_2O_3 system (TZP, polycrystalline tetragonal zirconia, with 3 mol% Y_2O_3 , vs YSZ/FSZ, yttria/fully stabilized zirconia, cubic, with 8–9 mol% Y_2O_3) [55, 56] but hardly considered in other systems. Ionic conductivities are not simply related to the dopant content. Structural and microstructural aspects play a major role in defect mobility and electrical conductivity.

Previous work on the electrical properties of zirconia-based materials focused on FSZ as fuel cell electrolyte to operate below 1000 °C [57–61]. For this purpose, a minor electronic transport is not an issue. Conversely, in Nernstian sensors this originates an internal short circuit current (ionic + electronic) and the electrolyte/electrode interfaces deviate from equilibrium. This is noticed at temperatures as low as 700–1000 °C when measuring low oxygen concentrations in the absence of buffer gas mixtures like H₂/H₂O or CO/CO₂ [62–66]. At higher temperature the effect is enhanced. Even so, possible operation outside the electrolytic domain is considered the main problem since the sensor signal departs from ideal [67–69].

As summary, Mg-PSZ are complex ceramic electrolytes where the C, T, and M phases might coexist. For a given chemical composition, exact phase compositions and microstructures change considerably with temperature and thermal history. The properties of M and T phases are in fact unknown but the global electrochemical performance of undoped materials, Mg-PSZ, Mg-FSZ, and allied electrolytes (all listed in Table 1) are available [54, 67, 69–96].

Data on undoped zirconia [70–76] will be used here for the first time as sensible source of information with respect to the electrochemical behavior of Mg-PSZ. In fact, for the ZrO₂–MgO system, the T phase below 1400 °C and the M phase below 1240 °C show negligible solid solution ranges, and their electrochemical performance should be somehow related to the corresponding performance of undoped materials.

Lastly, information obtained with dc and ac techniques will be combined in a complementary manner, to try to build a novel insight on the performance of these complex materials. To reach this goal, the remainder of this work is organized in the following sections: (i) materials; (ii) model ideal and real model performance; (iii) experimental techniques; (iv) sensor concepts; (v) electrochemical properties; (vi) concluding remarks.

2 Materials

As mentioned, the target of this work is the family of PSZ electrolytes, mostly MgO-doped. However, the selected list of materials is somewhat wider and preliminary comments are mandatory. All materials considered in this review, including acronyms, a short reference to chemical composition, phase content and firing conditions, can be found in Table 1. The organization of this table is based on chemical and phase composition to provide fast access to data sources. In this list we have firstly undoped zirconias, afterwards doped zirconia, lastly a few materials based on distinct oxides (e.g., HfO₂ or ThO₂) studied as alternatives to Mg-PSZ. According to the adopted notation, for

undoped ZrO₂ the acronym includes one first letter to identify the dominant phase (m or t for monoclinic or tetragonal, respectively) followed by the symbol Zr. When needed, a short reference to the first author and year of publication is included to specify distinct sources for the same material. As example, m-Zr (K1963) corresponds to undoped monoclinic ZrO₂ from a publication by Kofstad in 1963 [70]. For other materials the acronym also includes information on the chemical composition. As example, 9MgPSZ (Y1986) corresponds to a 9 mol% MgO-doped PSZ from a publication by Yamada in 1986 [82]. While Table 1 is a master list, Table 2 details exclusively available data on the conductivity of materials and corresponding activation energies according to their conductivity at 1600 °C. The rationale behind materials selection will be now detailed.

One first set of materials illustrate what could be classified as intrinsic behavior of zirconia [70–76]. In fact, undoped or lightly doped zirconia might be present in specific conditions in PSZ (e.g., below 1240 °C, see Fig. 1). So, the hereby named m-Zr and t-Zr are considered a reference, irrespective of their negligible technological relevance. Information available on the chemical composition of these materials shows that often they deviate from high purity. Foreign cations (e.g., Ca²⁺, Mg²⁺, Al³⁺ or Fe³⁺) in concentrations much higher than 100 ppm, easily acting as acceptor-like dopants, are often present (see Table 1). This should be kept in mind.

The widest group of materials is from the system ZrO₂–MgO [67, 69, 73, 77–85, 97]. This includes lightly doped materials, close to the single phase T field, but also heavily doped materials falling inside the single phase C field (Fig. 1). The borderline between PSZ and FSZ is vague since one material from the single C phase field might be cooled down in such a manner that the result is a mixture of phases. Thus, the adopted designations followed strictly the information provided by the authors. This explains why a 15 mol% MgO-doped zirconia is described as 15MgPSZ (95 wt% C [81]), while a 13.7 mol% MgO-doped material is designated as 13.7MgFSZ (100% C [85]).

CaO and CaO + MgO co-doped zirconia are also considered, corresponding to obvious attempts to tune the electrical performance using dopants with similar chemical characteristics [67, 86–92]. Still within zirconia-based materials, a few solid solutions with Y₂O₃ and HfO₂, with interesting performance were also considered [90, 93, 94]. Although also available, information on rare-earth dopants was mostly discarded. These materials are of little practical relevance.

Attempts to find suitable alternatives to PSZ included HfO₂ and ThO₂ as host oxides, due to their chemical analogy with respect to ZrO₂ [92, 95, 96]. Materials based on CaZrO₃ (with excess or deficit of CaO with respect to

Table 1 Materials considered in this work, including composition, firing conditions, acronyms and references

| Composition | | Acronym | Phases | Firing temperature (source) | References |
|------------------|--------------------------------|-------------------|--|-----------------------------|------------|
| Base oxide | Others (mol% unless specified) | | | | |
| ZrO ₂ | Hf-1.7 wt% | m-Zr (K1963) | M ⁽¹⁾ | 1400 °C | [70] |
| ZrO ₂ | Ca + Mg-400 ppm | m-Zr (V1964) | M ⁽¹⁾ | 2000 °C | [71] |
| ZrO ₂ | Ta < 200 ppm; Nb < 100 ppm | m-Zr (K1972) | M ⁽¹⁾ | 2200 °C | [72] |
| ZrO ₂ | <1 wt% | m-Zr (M1996) | M ⁽¹⁾ | 1650 °C | [73] |
| ZrO ₂ | Hf-1.7 wt% | t-Zr (K1963) | T ⁽²⁾ | 1400 °C | [70] |
| ZrO ₂ | Ca + Mg-400 ppm | t-Zr (V1965) | T ⁽²⁾ | 1800–2100 °C | [74] |
| ZrO ₂ | Fe-790 ppm; Al-125 ppm | t-Zr (M1966) | T ⁽²⁾ | >T _{Melting} | [75] |
| ZrO ₂ | n.r. | t-Zr (G1975) | T ⁽²⁾ | n.r. | [76] |
| ZrO ₂ | <1 wt% | t-Zr (M1996) | T ⁽²⁾ | 1650 °C | [73] |
| ZrO ₂ | MgO-3.2 | 3.2MgPSZ | >90 wt% M | 1650 °C | [73] |
| ZrO ₂ | MgO-4.7 | 4.7MgPSZ | n.r. | 1600 °C | [77] |
| ZrO ₂ | MgO-5 | 5MgPSZ | n.r. | n.r. | [78] |
| ZrO ₂ | MgO-5.1 | 5.1MgPSZ | 62 wt% M | 1650 °C | [73] |
| ZrO ₂ | MgO-6 | 6MgPSZ | n.r. | n.r. | [79] |
| ZrO ₂ | MgO-6.2 | 6.2MgPSZ | n.r. | 1600 °C | [77] |
| ZrO ₂ | MgO-6.8 | 6.8MgPSZ | 57 wt% M | 1650 °C | [73] |
| ZrO ₂ | MgO-7 | 7MgPSZ | C ⁽³⁾ + T ⁽²⁾ | n.r. | [67] |
| ZrO ₂ | MgO-7.5 | 7.5MgPSZ | 75 wt% M | 1600 °C | [80] |
| ZrO ₂ | MgO-7.6 | 7.6MgPSZ | n.r. | 1600 °C | [77] |
| ZrO ₂ | MgO-7.9 | 7.9MgPSZ | n.r. | 1600 °C | [77] |
| ZrO ₂ | MgO-8 | 8MgPSZ | 51 wt% M | 1650 °C | [73] |
| ZrO ₂ | MgO-3 wt% (8.6) | 8.6MgPSZ (V1988b) | C ⁽³⁾ (32 wt%) + T ⁽²⁾ | n.r. (a) | [54] |
| ZrO ₂ | MgO-9 | 9MgPSZ (I1984) | C ⁽³⁾ (40 wt%) + T ⁽²⁾ | n.r. (b) | [81] |
| ZrO ₂ | MgO-9 | 9MgPSZ (Y1986) | C ⁽³⁾ + T ⁽²⁾ | n.r. | [82] |
| ZrO ₂ | MgO-9 | 9MgPSZ (V1988a) | C ⁽³⁾ (25 wt%) + T ⁽²⁾ | n.r. (b) | [54] |
| ZrO ₂ | MgO-9 | 9MgPSZ (V1988c) | C ⁽³⁾ (25 wt%) + T ⁽²⁾ | n.r. (b) | [83] |
| ZrO ₂ | MgO-9 | 9MgPSZ (N1992) | C ⁽³⁾ + T ⁽²⁾ | n.r. (c) | [69] |
| ZrO ₂ | MgO-9 | 9MgPSZ (Y2013) | C ⁽³⁾ + T ⁽²⁾ + M ⁽¹⁾ | 1600 °C | [97] |
| ZrO ₂ | MgO-3.4 wt% (9.7) | 9.7MgPSZ (M1995) | 8–67 wt% M | 1600 °C | [84] |
| ZrO ₂ | MgO-9.7 | 9.7MgPSZ (T1986) | M < 15 wt% | 1600 °C | [77] |
| ZrO ₂ | MgO-11.4 | 11.4MgPSZ (T1986) | M < 15 wt% | 1600 °C | [77] |
| ZrO ₂ | MgO-11.9 | 11.9MgPSZ (M1996) | 16 wt% M | 1650 °C | [73] |
| ZrO ₂ | MgO-11.9 | 11.9MgPSZ (M1998) | 28 wt% M | 1600 °C | [80] |
| ZrO ₂ | MgO-13.7 | 13.7MgFSZ (M1995) | C ⁽³⁾ | 1650 °C | [85] |
| ZrO ₂ | MgO-13.7 | 13.7MgFSZ (M1996) | C ⁽³⁾ | 1650 °C | [73] |
| ZrO ₂ | MgO-15 | 15MgPSZ | C ⁽³⁾ (95 wt%) + T ⁽²⁾ | n.r. (b) | [81] |
| ZrO ₂ | CaO-8 | 8CaPSZ | C ⁽³⁾ + T ⁽²⁾ + M ⁽¹⁾ | 1830 °C | [86] |
| ZrO ₂ | CaO-11 | 11CaPSZ (I1981a) | n.r. | n.r. | [87] |
| ZrO ₂ | CaO-11 | 11CaPSZ (I1981b) | n.r. | n.r. | [68] |
| ZrO ₂ | CaO-12 | 12CaPSZ | n.r. | n.r. (d) | [88] |
| ZrO ₂ | CaO-13 | 13CaPSZ (J1979) | C ⁽³⁾ + T ⁽²⁾ | n.r. | [67] |
| ZrO ₂ | CaO-13 | 13CaPSZ (D1979) | C ⁽³⁾ + T ⁽²⁾ | n.r. | [89] |
| ZrO ₂ | CaO-14 | 14CaPSZ | C ⁽³⁾ + T ⁽²⁾ | 1700 °C | [90] |
| ZrO ₂ | CaO-30 | 30CaSZ (T1964) | C ⁽³⁾ + CaZrO ₃ | n.r. | [91] |
| ZrO ₂ | CaO-30 | 30CaSZ (D2008) | C ⁽³⁾ + CaZrO ₃ | n.r. | [89] |
| ZrO ₂ | MgO-3.2, CaO-6.6 | 3.2Mg6.6CaPSZ | C ⁽³⁾ + T ⁽²⁾ + M ⁽¹⁾ | 1830 °C | [86] |
| ZrO ₂ | MgO-4.7, CaO-11.3 | 4.7Mg11.3Ca84Zr | n.r. | n.r. | [92] |

Table 1 continued

| Composition | | Acronym | Phases | Firing temperature (source) | References |
|--------------------|---|-----------------|-------------------------------------|-----------------------------|------------|
| Base oxide | Others (mol% unless specified) | | | | |
| ZrO ₂ | Y ₂ O ₃ -1.4 | 1.4Y(2)98.6Zr | T ⁽²⁾ | 1300–1400 °C | [93] |
| ZrO ₂ | Y ₂ O ₃ -8 | 8Y(2)92Zr | n.r. | n.r. | [94] |
| ZrO ₂ | Y ₂ O ₃ -25 | 25Y(2)75Zr | C ⁽³⁾ | 1700 °C | [90] |
| ZrO ₂ | HfO ₂ -35, Y ₂ O ₃ -25 | 35Hf(25Y(2)40Zr | C ⁽³⁾ | 1700 °C | [95] |
| HfO ₂ | CaO-12 | 12Ca88Hf | n.r. | n.r. | [92] |
| HfO ₂ | CaO-16.5 | 16.5Ca83.5Hf | M ⁽¹⁾ + C ⁽³⁾ | 1700 °C | [95] |
| HfO ₂ | Y ₂ O ₃ -10 | 10Y(2)90Hf | M ⁽¹⁾ + C ⁽³⁾ | 1700 °C | [95] |
| HfO ₂ | Y ₂ O ₃ -20 | 20Y(2)80Hf | C ⁽³⁾ | 1700 °C | [95] |
| HfO ₂ | Gd ₂ O ₃ -35 | 35Gd(2)65Hf | Pyr ⁽⁴⁾ | 1700 °C | [95] |
| HfO ₂ | ThO ₂ -8, Y ₂ O ₃ -12 | 8Th12Y(2)80Hf | C ⁽³⁾ + ThO ₂ | 2000 °C | [95] |
| ThO ₂ | Y ₂ O ₃ -8 | 8Y(2)92Th | n.r. | n.r. | [96] |
| CaZrO ₃ | CaO-45 | 45Ca55Zr | Per(o) ⁽⁵⁾ | n.r. | [89] |
| CaZrO ₃ | CaO-46 | 46Ca54Zr | Per(o) ⁽⁵⁾ | n.r. | [92] |
| CaZrO ₃ | CaO-47 | 47Ca53Zr | Per(o) ⁽⁵⁾ | n.r. | [79] |
| CaZrO ₃ | CaO-48 | 48Ca52Zr | Per(o) ⁽⁵⁾ | n.r. | [89] |
| CaZrO ₃ | CaO-50 | 50Ca50Zr | Per(o) ⁽⁵⁾ | n.r. | [89] |
| CaZrO ₃ | CaO-52 | 52Ca48Zr | Per(o) ⁽⁵⁾ | n.r. | [92] |
| CaZrO ₃ | CaO-54 | 54Ca46Zr | Per(o) ⁽⁵⁾ | n.r. | [79] |

⁽¹⁾ Monoclinic; ⁽²⁾ tetragonal; ⁽³⁾ cubic (fluorite); ⁽⁴⁾ pyrochlore; ⁽⁵⁾ perovskite (orthorhombic), with the likely presence of a secondary phase when the atomic ratio Ca/Zr is different from 1; (a) Corning; (b) Nippon Kagaku Tokyo Co. Ltd.; (c) Nikkato; (d) Nippon Chem. Cer. Co. Ltd *n.r.* not reported

the ideal stoichiometry) were also considered in the present survey [79, 89, 92]. With this last collection of examples emphasis is still on compositions based on oxides from the IVB group and alkaline-earth metal oxides but the few extra cases ensured also the coverage of distinct crystal structures (pyrochlores and perovskites).

3 Model ideal and real performance

The efficacy of one oxygen sensor relies strongly on the electrolyte material, namely on the relative levels of ionic and electronic conductivity. Key relations on electrolyte materials and sensor performance will be recalled in the following paragraphs.

The open circuit voltage (*V*) observed in a mixed conducting cell (ionic and electronic) when exposed to an oxygen pressure (pO₂) gradient can be calculated from the traditional relation [98]:

$$V = \frac{RT}{4F} \int t_i d(\ln pO_2), \tag{1}$$

where *t_i* is the ionic transport number, *R* and *F* the gas and Faraday constants, and *T* the absolute temperature, respectively. By definition

$$t_i = \frac{\sigma_i}{\sigma_i + \sigma_e}, \tag{2}$$

where σ_i and σ_e are the ionic and electronic conductivities, respectively.

The integration limits in Eq. (1) are the higher and lower oxygen partial pressures in contact with the cell/sensor walls (*P_H* and *P_L*, respectively). For pure electrolytes (*t_i* ≈ 1), this yields the well-known ideal (thermodynamic) Nernstian voltage (*V_o*):

$$V_o = \frac{RT}{4F} \ln \frac{P_H}{P_L}. \tag{3}$$

In typical oxygen sensors *P_H* is usually the so-called reference oxygen partial pressure, established using a gas with known oxygen content (e.g., air) or a metal/metal oxide couple acting as a buffer with respect to pO₂, assuming chemical equilibrium between solid phases and gas. Accordingly, knowing *T*, any voltage reading is a direct measure of *P_L*, the unknown oxygen pressure.

For typical zirconia-doped materials where a constant concentration of ionic charge carriers is usually determined by the dopant concentration, the ionic conductivity is constant and the electronic contributions depend on pO₂^{-1/4} (n-type) and pO₂^{1/4} (p-type). In this case one may write the generic relation for the electronic conductivity:

Table 2 Conductivity (σ) at 1600 °C and activation energies (E_a) for distinct electrolyte materials (t-Zr also included)

| Base oxide | Dopants or main impurities (mol%) | Acronym | σ cm/S | | E_a (eV) | References |
|------------------|-----------------------------------|-----------------|------------------------------------|------------------------|------------|------------|
| | | | Range | Value | | |
| ZrO ₂ | n.r. | t-Zr (G1975) | <10 ⁻² | 4.6 × 10 ⁻³ | – | [76] |
| ZrO ₂ | CaO-50 | 50Ca50Zr | | 5.1 × 10 ⁻³ | 2.25 | [89] |
| ZrO ₂ | CaO-48 | 48Ca52Zr | 10 ⁻² –10 ⁻¹ | 2.8 × 10 ⁻² | 1.37 | [89] |
| ZrO ₂ | CaO-54 | 54Ca46Zr | | 3.0 × 10 ⁻² | 1.74 | [79] |
| ZrO ₂ | CaO-52 | 52Ca48Zr | | 5.6 × 10 ⁻² | 2.30 | [92] |
| ZrO ₂ | CaO-45 | 45Ca55Zr | | 5.8 × 10 ⁻² | 1.34 | [89] |
| ZrO ₂ | CaO-46 | 46Ca54Zr | | 5.8 × 10 ⁻² | 2.02 | [92] |
| ZrO ₂ | CaO-47 | 47Ca53Zr | | 7.0 × 10 ⁻² | 1.92 | [79] |
| ZrO ₂ | MgO-5 | 5MgPSZ | >10 ⁻¹ | 1.3 × 10 ⁻¹ | 0.67 | [78] |
| ZrO ₂ | MgO-7 | 7MgPSZ | | 1.3 × 10 ⁻¹ | 0.67 | [67] |
| ThO ₂ | Y ₂ O ₃ -8 | 8Y(2)92Th | | 1.4 × 10 ⁻¹ | 1.00 | [67] |
| ZrO ₂ | MgO-9 | 9MgPSZ (N1992) | | 1.6 × 10 ⁻¹ | – | [69] |
| HfO ₂ | CaO-12 | 12Ca88Hf | | 2.6 × 10 ⁻¹ | 1.43 | [92] |
| ZrO ₂ | CaO-30 | 30CaSZ | | 3.2 × 10 ⁻¹ | 1.33 | [89] |
| ZrO ₂ | CaO-12 | 12CaPSZ | | 3.9 × 10 ⁻¹ | 1.25 | [88] |
| ZrO ₂ | MgO-4.7; CaO-11.3 | 4.7Mg11.3Ca84Zr | | 6.0 × 10 ⁻¹ | 0.68 | [92] |
| ZrO ₂ | CaO-13 | 13CaPSZ (J1979) | | 6.0 × 10 ⁻¹ | 0.68 | [67] |
| ZrO ₂ | CaO-13 | 13CaPSZ (D2008) | | 6.0 × 10 ⁻¹ | 0.72 | [89] |
| ZrO ₂ | Y ₂ O ₃ -8 | 8Y(2)92Zr | | 6.0 × 10 ⁻¹ | 0.70 | [94] |

$$\sigma_e = \sigma_n^o \cdot pO_2^{-1/4} + \sigma_p^o \cdot pO_2^{1/4}, \quad (4)$$

where σ_n^o and σ_p^o are the n-type and p-type contributions extrapolated to unit oxygen partial pressure. For a zirconia-based electrolyte material behaving in such an ideal manner, the total conductivity (σ_t) shows the following pO_2 dependence [99–101]:

$$\sigma_t = \sigma_i + \sigma_n^o \cdot pO_2^{-1/4} + \sigma_p^o \cdot pO_2^{1/4}. \quad (5)$$

According to Eq. (5), standard plots of $\log \sigma_t$ versus $\log pO_2$ should reveal a branch with a slope of $-1/4$ under extremely low oxygen partial pressures, an intermediate range of pO_2 with constant conductivity and a branch with a slope of $+1/4$ at extremely high values of pO_2 . Figure 2, based on published data for Ca-doped PSZ [88], shows one typical plot where the meaning of all these symbols and trends are easily perceived.

For materials like Mg-PSZ or YSZ this model performance is widely accepted. However, Eq. (5) will be also used to analyze sets of data on total conductivity as a function of pO_2 for undoped zirconia (m-Zr or t-Zr), even if slightly distinct experimental slopes (e.g., $+1/5$ or $-1/6$) were also reported [70–72, 74–76, 102]. Accordingly, the adequacy of this solution will be discussed in due time.

The ionic transport number can be obtained combining Eqs. (2) and (4):

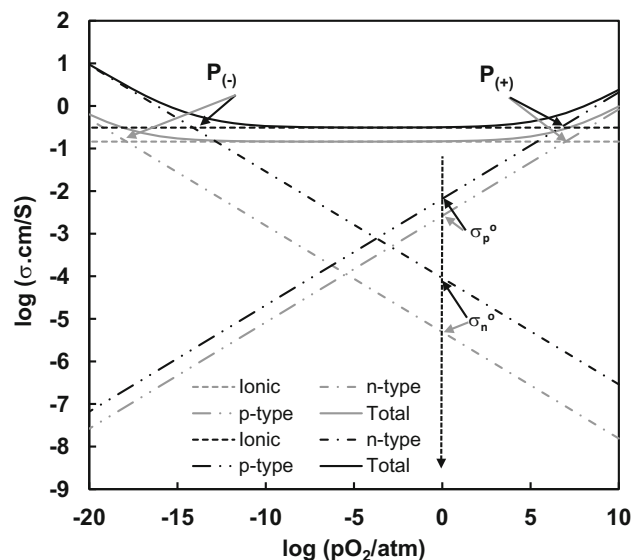


Fig. 2 Log–log plot of the pO_2 dependence of the ionic, n-type and p-type conductivity in 12CaPSZ at 1662 (grey lines) and 1820 (black lines) K, from published data [88]. Also pinpointed the values of $P_{(-)}$, $P_{(+)}$, σ_n^o and σ_p^o . See main text for the meaning of the symbols

$$t_i = \frac{1}{1 + A \cdot pO_2^{-1/4} + B \cdot pO_2^{1/4}}. \quad (6)$$

Here $A = \sigma_n^o/\sigma_i$ is the n-type to ionic conductivity ratio (extrapolated) for unit oxygen partial pressure, and $B = \sigma_p^o/\sigma_i$

σ_i is the analogous ratio for the p-type to ionic conductivity. Since A and B are constants (only temperature dependent), this type of expression for t_i facilitates the calculation of the integral shown in Eq. (1). Furthermore, under typical sensor working conditions the p-type conductivity of zirconia-based materials is usually small. In this case, the ionic transport number can be further reduced to:

$$t_i = \frac{1}{1 + A \cdot pO_2^{-1/4}} \tag{7}$$

Integration of Eq. (1) after incorporation of Eq. (7), gives [101]:

$$V = \frac{RT}{4F} \ln \frac{P_H}{P_L} + \frac{RT}{F} \ln \frac{1 + A \cdot P_H^{-1/4}}{1 + A \cdot P_L^{-1/4}} \tag{8}$$

This expression conveniently separates the terms corresponding to ideal and non-ideal performance. In fact, the right hand side of Eq. (8) includes one first term corresponding to the ideal Nernstian sensor voltage (Eq. 3), and one second term describing the deviation from ideal behavior. Another expression frequently found in the literature for the sensor reading is (e.g., [79, 91, 105, 106]):

$$V = \frac{RT}{F} \ln \frac{P_H^{1/4} + P_{(-)}^{1/4}}{P_L^{1/4} + P_{(-)}^{1/4}} \tag{9}$$

In this case $P_{(-)}$ corresponds to the so-called lower limit of the ionic domain, when $t_i = 0.5$ or $\sigma_i = \sigma_n$. From the adopted definitions, $A = P_{(-)}^{1/4}$. Proper handling of these relations easily shows that Eqs. (8) and (9) are identical.

Figure 3 shows the predictable dependence of the sensor voltage on $P_{(-)}$, using Eq. (9). The straight line corresponds to Eq. (3), as such depending exclusively on the sensor boundary conditions and temperature. Curves corresponding to the deviation from Eq. (3) are also shown in Fig. 3. The value for P_H was set (10^{-14} atm) within the order of magnitude of the equilibrium pO_2 at 1500 °C for the couple Cr/Cr₂O₃, often used as reference electrode [103, 104]. Two $P_{(-)}$ values (10^{-16} and 10^{-18} atm) were also selected from typical data ranges reported for PSZ materials at the same temperature.

Figure 3 clearly shows that the lower $P_{(-)}$ the higher the accuracy in the sensor readings. However, for measurements at low oxygen partial pressures (e.g., $P_L < 10^{-16}$ atm, corresponding to oxygen activities in molten steel below 1 ppm, at 1500 °C) deviation between ideal and real sensor signals might be as high as 40%. These comments showed that $P_{(-)}$ is a good parameter for benchmarking purposes when talking about electrolytes for oxygen sensors. In fact, reports on the high temperature (1200–1600 °C) performance of materials for oxygen sensors

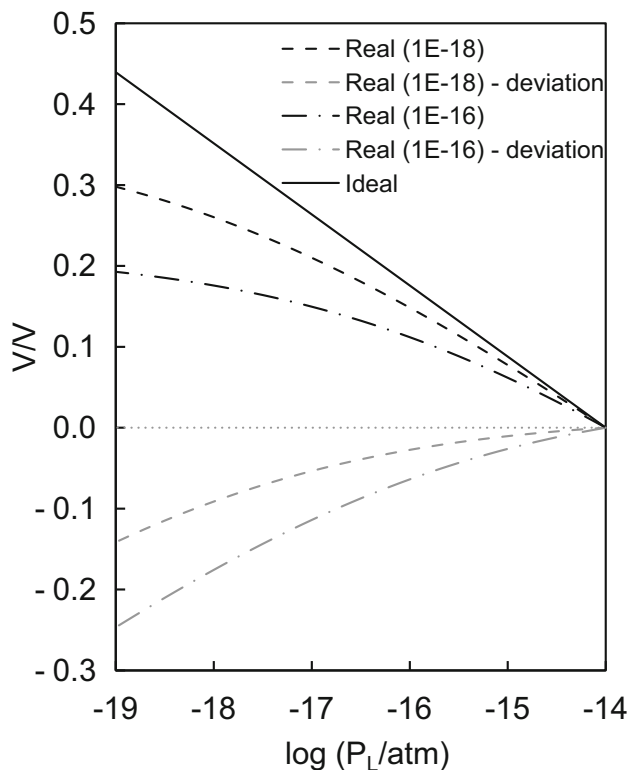


Fig. 3 Simulated voltage (V) readings as a function of P_L , assuming sensors obeying either Eq. (3) (ideal, irrelevant electronic conductivity) or Eq. (9) (real, significant electronic conductivity). In the latter case two distinct values of $P_{(-)}$ were assumed (shown in the inner caption). Deviation between real and ideal readings is also shown. See text for remaining details

consist usually of listings of values of $P_{(-)}$ at distinct temperatures, or the regression parameters obtained for the equation (e.g., [77–79, 89, 91–93]):

$$\log P_{(-)} = A + \frac{B}{T} \tag{10}$$

The analysis of competitive materials will be thus centered on $P_{(-)}$, essential in electrolyte benchmarking. Table 3 includes a collection of $P_{(-)}$ values at 1600 °C for a number of electrolyte materials, sorted according to their magnitude. Simple analysis of this listing shows that known $P_{(-)}$ values cover several orders of magnitude.

4 Experimental techniques

Data considered in this work was obtained using a wide range of experimental techniques and conditions, including both dc (direct current) and ac (alternate current) measurements. With respect to ac techniques, conditions involved constant frequency conductivity measurements as well as impedance spectroscopy. The limitations of dc or constant frequency measurements with respect to impedance spectroscopy are

Table 3 $P_{(-)}$ values at 1600 °C for selected electrolyte materials (t-Zr also included)

| Base oxide | Dopants or main impurities (mol% unless specified) | Acronym | $P_{(-)}$ at 1600 °C (atm) | | References |
|--------------------|---|-------------------|--------------------------------------|-------------------------|------------|
| | | | Range | Value | |
| ZrO ₂ | n.r. | t-Zr (G1975) | >10 ⁻¹¹ | 4.8 × 10 ⁻¹¹ | [76] |
| ZrO ₂ | Ca + Mg-400 ppm | t-Zr (V1965) | | 3.2 × 10 ⁻¹¹ | [74] |
| ZrO ₂ | MgO-9 | 9MgPSZ (N1992) | 10 ⁻¹³ –10 ⁻¹⁴ | 7.1 × 10 ⁻¹⁴ | [69] |
| ZrO ₂ | MgO-9 | 9MgPSZ (V1988a) | | 3.4 × 10 ⁻¹⁴ | [54] |
| ZrO ₂ | MgO-9 | 9MgPSZ (V1988c) | | 3.1 × 10 ⁻¹⁴ | [83] |
| ZrO ₂ | MgO-8.6 | 8.6MgPSZ (V1988b) | | 2.4 × 10 ⁻¹⁴ | [54] |
| ZrO ₂ | MgO-9 | 9MgPSZ (I1984) | 10 ⁻¹⁴ –10 ⁻¹⁵ | 9.1 × 10 ⁻¹⁵ | [81] |
| ZrO ₂ | MgO-15 | 15MgPSZ (I1984) | | 4.2 × 10 ⁻¹⁵ | [81] |
| ZrO ₂ | MgO-9 | 9MgPSZ (Y1986) | | 3.2 × 10 ⁻¹⁵ | [82] |
| ZrO ₂ | MgO-4.7, CaO-11.3 | 4.7Mg11.3Ca84Zr | | 1.2 × 10 ⁻¹⁵ | [92] |
| ZrO ₂ | CaO-13 | 13CaPSZ (J1979) | | 1.2 × 10 ⁻¹⁵ | [79] |
| ZrO ₂ | CaO-11 | 11CaPSZ (I1981b) | | 1.0 × 10 ⁻¹⁵ | [68] |
| ZrO ₂ | CaO-15 | 15CaPSZ | 10 ⁻¹⁵ –10 ⁻¹⁶ | 7.4 × 10 ⁻¹⁶ | [81] |
| ZrO ₂ | MgO-6 | 6MgPSZ (J1977) | | 5.2 × 10 ⁻¹⁶ | [79] |
| ZrO ₂ | MgO-5 | 5MgPSZ | | 5.2 × 10 ⁻¹⁶ | [94] |
| ZrO ₂ | MgO-7 | 7MgPSZ (J1979) | | 5.1 × 10 ⁻¹⁶ | [92] |
| ZrO ₂ | CaO-14 | 14CaPSZ | | 4.8 × 10 ⁻¹⁶ | [90] |
| ZrO ₂ | Y ₂ O ₃ -10 | 10Y(2)90Zr | | 4.2 × 10 ⁻¹⁶ | [94] |
| ZrO ₂ | Y ₂ O ₃ -8 | 8Y(2)92Zr | | 4.0 × 10 ⁻¹⁶ | [94] |
| HfO ₂ | CaO-16.5 | 16.5Ca83.5Hf | 10 ⁻¹⁷ –10 ⁻¹⁸ | 9.1 × 10 ⁻¹⁸ | [92] |
| ZrO ₂ | Y ₂ O ₃ -25 | 25Y(2)75Zr | | 7.9 × 10 ⁻¹⁸ | [90] |
| HfO ₂ | Y ₂ O ₃ -10 | 10Y(2)90Hf | | 7.8 × 10 ⁻¹⁸ | [95] |
| HfO ₂ | Gd ₂ O ₃ -35 | 35Gd(2)65Hf | | 2.0 × 10 ⁻¹⁸ | [95] |
| CaZrO ₃ | CaO-52 | 52Ca48Zr | | 1.5 × 10 ⁻¹⁸ | [92] |
| CaZrO ₃ | CaO-46 | 46Ca54Zr | | 1.4 × 10 ⁻¹⁸ | [92] |
| ThO ₂ | Y ₂ O ₃ -8 | 8Y(2)92Th | | 1.2 × 10 ⁻¹⁸ | [79] |
| ZrO ₂ | HfO ₂ -35, Y ₂ O ₃ -25 | 35Hf25Y(2)40Zr | | 1.2 × 10 ⁻¹⁸ | [95] |
| HfO ₂ | ThO ₂ -8, Y ₂ O ₃ -12 | 8Th12Y(2)80Hf | 10 ⁻¹⁸ –10 ⁻¹⁹ | 2.3 × 10 ⁻¹⁹ | [95] |
| HfO ₂ | Y ₂ O ₃ -20 | 20Y(2)80Hf | | 1.4 × 10 ⁻¹⁹ | [95] |

well known, but data on these materials were often obtained in the 1960s–1970s, and impedance spectroscopy as a characterization tool for high temperature solid electrolytes was only slowly adopted after the pioneering work of Bauerle [105]. This means that even constant frequency conductivity data might not describe the total or bulk conductivity of a given material throughout all experimental conditions (e.g., temperature and/or pO₂). In the case of dc conductivity measurements the problem is obviously worst. This might explain apparently abnormal fluctuations in a few reported sets of data, with one of such examples shown in Fig. 4, for m-Zr at 1000 °C. In the oxygen partial pressure range 10⁻⁵–1 atm, the usual tendency for increasing p-type conductivity with increasing pO₂ seems temporarily reversed before being obeyed again. As guidance on the relative orders of magnitudes of conductivity for the distinct

materials, the maximum conductivity reported for Mg-PSZ at 1000 °C was in the order of 0.03 S/cm (log (σ cm/S) = -1.5, with about 8 mol% MgO) [77]. This value is much higher (three orders of magnitude) than for m-Zr and in the order of magnitude of the total conductivity of t-Zr at 1600 °C.

As limitations in reported data we should also realize that nowadays widely used painted metal electrodes were by no means a standard procedure in the past. Some reports indicate simple contact (under pressure) between disks acting as electrodes and pellets under scrutiny [70, 72, 75]. Instability of readings was noticed [75]. All these limitations are mostly found in measurements involving undoped zirconia and might also explain the mismatch in magnitude found in a few cases for one same material and similar experimental conditions (Fig. 4).

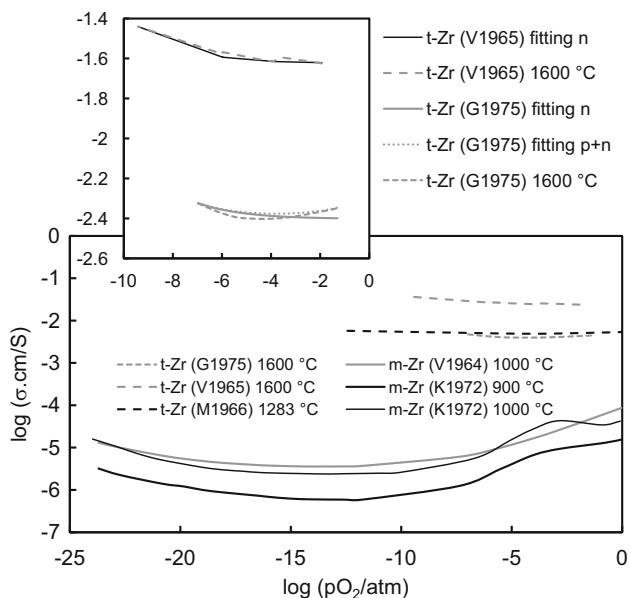
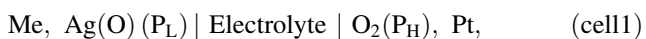


Fig. 4 Log–log plots of the dependence of the conductivity (σ) of nominally pure zirconia on the oxygen partial pressure (pO_2), at distinct temperatures, for selected sets of literature data. The *inset* shows two examples of data fitting assuming only n-type or n- and p-type contributions besides the ionic contribution (Eq. 5). Temperatures shown in the inner caption. Data sources can be found in Table 1

Besides these experimental limitations, the solutions used to study electrolyte materials for oxygen sensors included inventive and often complex cells and procedures for data analysis, detailed in the following paragraphs.

4.1 Characterization by dc techniques

As previously mentioned, one of the critical parameters in the scrutiny of electrolyte materials for oxygen sensors is $P_{(-)}$. This parameter might be obtained from log–log plots of total conductivity versus pO_2 , using Eq. (5) to fit experimental data and extract the required information on ionic and electronic conductivity. However, most results were obtained from open circuit voltage readings in cells such as [69, 79, 81, 106, 107]:

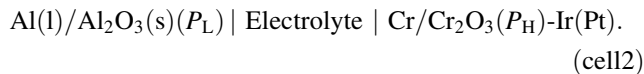


where P_L and P_H are the boundary oxygen partial pressures in equilibrium with the sensor, and Me and Pt the electrical wires (e.g., Me = Mo or W) used in these measurements. Here, atmospheres in contact with the Pt electrode should be rich in oxygen (e.g., $P_H = 1$ atm). On the contrary, based on a forced dc current used to remove oxygen from the (molten) Ag electrode, P_L could be driven to values well below $P_{(-)}$. In such circumstances, Eq. (9) can be reduced to:

$$V = \frac{RT}{4F} \ln \frac{P_H}{P_{(-)}}. \quad (11)$$

The voltage reading in such circumstances can be used to estimate the value of $P_{(-)}$. This experimental solution, named as coulometric titration, was firstly introduced to study the ionic domain of single and double layer electrolytes [108, 109].

Alternative solutions to estimate $P_{(-)}$ involved also oxygen concentration cells where both boundary conditions were determined by metal/metal oxide coexistence electrodes, namely the Cr/Cr₂O₃ and Al/Al₂O₃ couples [95]:



While the equilibrium oxygen partial pressure for the Cr-based electrode is within the ionic domain of standard Mg-PSZ materials, the corresponding value for the Al-based electrode is clearly below the lower limit of the ionic domain [95]. In this manner, the cell voltage reading can again be used to estimate $P_{(-)}$ using Eq. (9) and tabulated data on the equilibrium oxygen partial pressures in the metal/metal oxide electrodes. The exact combination of electrode materials (or cell boundary conditions) might be changed but in essence data must be handled using Eqs. (9) or (11).

An interesting alternative to assess $P_{(-)}$ involved simultaneous measurements in molten steel with low oxygen activity, using sensors with distinct reference electrodes (Cr and Mo-based, respectively) [110]. Proper simultaneous handling of Eq. (9) for two distinct reference electrodes easily shows that in this manner $P_{(-)}$ can be estimated ignoring the exact oxygen activity in the melt.

4.2 Characterization by ac techniques

Besides constant frequency ac conductivity measurements, with the limitations already noticed, impedance spectroscopy was used more recently to inspect a variety of PSZ materials [73, 77, 80, 84–86]. Data obtained within typical temperature ranges (up to 300–600 °C), where impedance spectra often show key details (like bulk and grain boundary arcs) cannot be extrapolated to actual sensor operating conditions (>1400 °C). Also, as PSZ materials are metastable, their phase content and electrical performance easily drift during measurements [73, 84]. Furthermore, coexistence of three phases and intricate microstructures should be kept in mind, including dispersed precipitates of a T phase (and/or M phase) within large C matrix grains, and islands of small M grains between large C grains (e.g., [11, 14, 20, 24, 86]). While these constraints are obvious, the potential of impedance spectroscopy at low temperature to assess the condition of these materials should not be discarded.

Figure 5 shows a set of examples of impedance spectra obtained with undoped zirconia, covering m-Zr and t-Zr. The resulting Arrhenius-type temperature dependence for the electrical conductivity is shown in Fig. 5b, where the shift from m-Zr to t-Zr is within the range of temperatures usually reported [73]. In Fig. 5a we can immediately realize that the same material might reveal distinct microstructural features depending on temperature. For m-Zr bulk and grain boundary arcs are strongly overlapped. The presence of a grain boundary contribution can be understood from the decreasing curvature of the impedance spectra in the frequency range below 10^4 Hz. On the contrary, for t-Zr the presence of two arcs is clear, with the bulk arc ending around $Z' = 0.85$, and the grain boundary arc extending from here to $Z' = 1$ (Fig. 5a). The overall differences might indicate that the balance between ionic

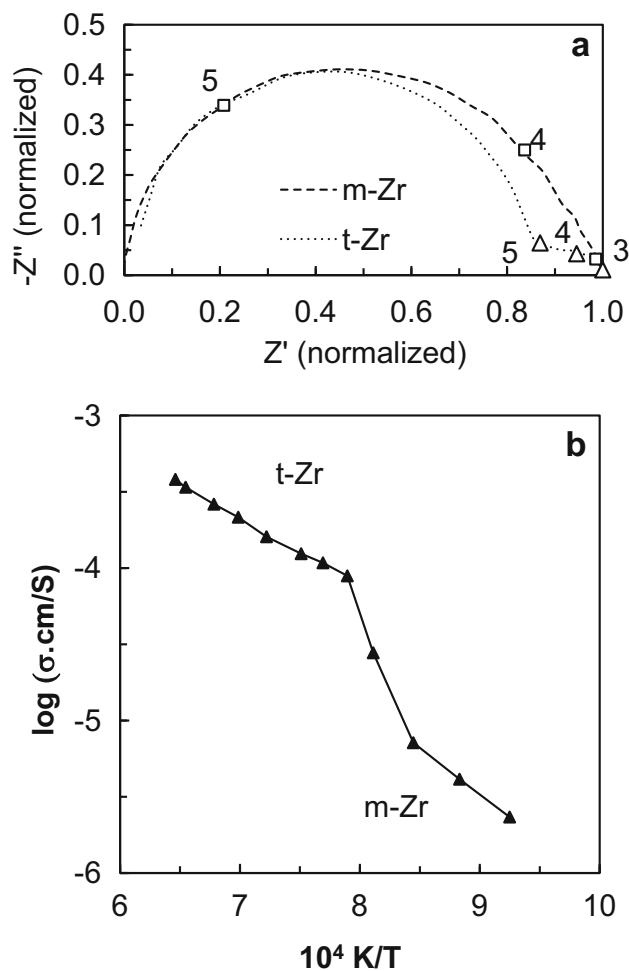


Fig. 5 Normalized impedance spectroscopy data (a) and dependence of the $\log \sigma$ on the reciprocal of the absolute temperature (b) for undoped m-Zr and t-Zr materials. In (a) numbers indicate the logarithms of the measuring frequency (Hz) for a few points. Impedance data collected at 1211 K for m-Zr and 1546 K for t-Zr. Adapted from [73]

and electronic transport is changing with temperature, with ionic transport more relevant in t-Zr. In fact, these data were obtained from the same specimen, only temperature changed. Furthermore, measurements after 15 h equilibration provided similar results [73].

While for single phase undoped materials the situation is easily handled, inventive attempts to apply impedance spectroscopy to study Mg-PSZ deserve some reference. These included efforts to simplify the system, with annealing and thermal cycling to ensure the T to M conversion, while the C phase was mostly preserved [73, 84–86]. On changing the composition of Mg-PSZ materials and the corresponding M phase content, impedance spectra showed wide changes in shape and magnitude (Fig. 6a). From these data a clear correlation could be obtained between the M phase content and the so-called blocking effect of this insulating phase with respect to ionic transport [73].

This treatment followed previous work addressing the effect of microstructural defects on impedance spectra of ceramic electrolytes [111]. According to the adopted model, in C + M materials any blocking particle must originate “dead regions” (blocked zones) with respect to ionic transport (Fig. 6b), and one extra arc should be seen as the response of a blocked RC circuit in which the capacitance C is associated with an ‘average’ isolating M grain of area S and thickness t. Therefore,

$$C = \varepsilon \varepsilon^0 S t^{-1}. \quad (12)$$

Here ε^0 and ε are, respectively, the vacuum permittivity and the relative permittivity of M zirconia. The resistance R stands for the part of the conducting matrix blocked by the capacitance, where the volume is assumed to be approximately proportional to the blocker surface area (thickness only temperature dependent), and can be written as:

$$R \propto \rho S^{-1} \quad (13)$$

with ρ the conducting matrix resistivity. For the relaxation frequency (f) of the extra arc obeying the standard equation:

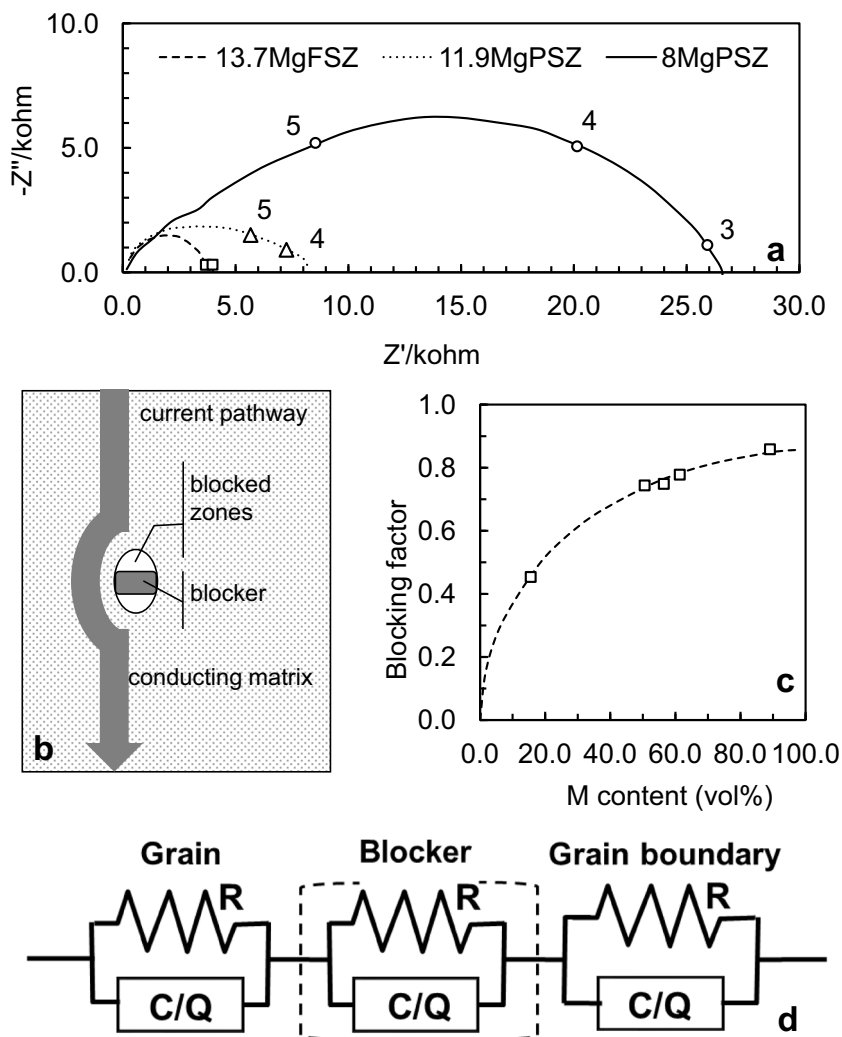
$$f = (2\pi RC)^{-1} \quad (14)$$

the result should be:

$$f \propto (\varepsilon \varepsilon^0 \rho t^{-1})^{-1}. \quad (15)$$

The resistance and relaxation frequency associated with the blocking process exhibited activation energies very close to that of the matrix resistivity, in agreement with the above equations, supporting the above assumptions. The blocking factor, α_R , measuring the fraction of blocked ionic carriers, used to quantify the role of M particles in the

Fig. 6 **a** Impedance spectroscopy data at 780 K for distinct Mg-doped materials; **b** schematic description of the ion-blocking effect due to the presence of M zirconia grains; **c** dependence of the blocking factor on the estimated M phase content; **d** equivalent circuit considering the role of the blocking phase (see text for details). In **(a)** numbers indicate the logarithms of the measuring frequency (Hz) for a few points. Adapted from [73]



system, also increased consistently with the M phase content (Fig. 6c).

An equivalent circuit able to take into consideration the role of the blocking phase is shown in Fig. 6d, including typical circuit elements (R , C , Q) used in similar analyses. Here Q stands for a constant phase element. Consideration of parallel RQ elements is quite effective in the analysis of spectra involving depressed arcs, although these might be equally described as off-centered semicircles (below the Z' axis) corresponding to the response of a parallel RC circuit. In materials with high blocking effects, the arc corresponding to the blocker dominated over the grain boundary arc. For minor blocking effects the extra arc vanishes and the equivalent circuit shows only the classical bulk and grain boundary arcs.

Impedance spectroscopy measurements were also carried out in specimens before and after thermal shock from 1600 °C to room temperature (Fig. 7) [80]. Before thermal shock Mg-PSZ specimens showed somewhat fuzzy impedance spectra, with strongly overlapping contributions at

high and intermediate frequencies, in line with some results presented in Fig. 6a. However, after thermal shock, the higher frequency arc was revealed, indicating that the content of less resistive phases (C and/or T) increased at the expense of the blocking phase (M). For 11.9MgPSZ, the impedance diagram after thermal shock is typical of FSZ, presenting well resolved arcs due to inter- and intra-grain resistivities. Moreover, after thermal shock the intra-grain resistivity is higher than before, suggesting that the T phase is less resistive than the C one (there is no T phase after thermal shock), as pinpointed in Fig. 7 with horizontal arrows [80]. This is one of several interesting clues on the relative magnitudes of conductivity in the T and C phases in Mg-PSZ.

Attempts to discriminate the electrical conductivity contributions from all coexisting phases require more complex assumptions. The only documented possibility invoked the model for the electrical performance of an insulating dispersed phase within a conducting matrix [86]. With prolonged annealing PSZ shifted from $C + T$ to

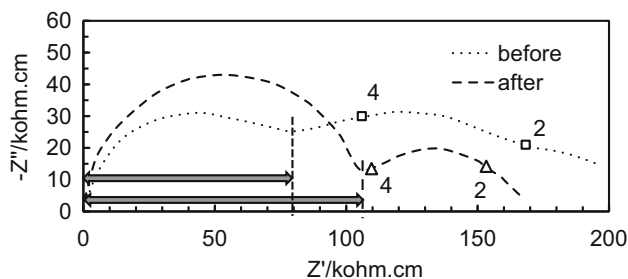


Fig. 7 Impedance spectroscopy data at 780 K for 11.9MgPSZ before and after thermal shock from 1873 K to room temperature. Numbers indicate the logarithms of the measuring frequency (Hz) for a few points. Horizontal arrows pinpoint the shift in magnitude of the high frequency arc. Adapted from [80]

C + M. The resistivity of the grain interior, obtained from impedance plots, showed three stages of behavior. The first stage was attributed to the equilibration of samples with respect to their C + T phase content, since before annealing the samples were cooled from sintering (1830 °C) to room temperature. The second stage involved coarsening of the T phase, while the last stage included the transformation of T phase precipitates into the resistive M phase. This analysis showed that at low temperature the order of magnitude of estimated conductivities obeyed the sequence $T > C > M$, in line with the previous comment on the relative magnitude of the conductivity of the T and C phases. Obviously, handling of these data was far from trivial and unambiguous. Available models apply to specific geometries of dispersed phases and volume fractions, not necessarily observed in all circumstances.

5 Sensor concepts

Sensor concepts will be shortly mentioned here to emphasize the combined role of materials' properties and design parameters (shape, dimensions). The most widely used sensor concept corresponds to a closed end tube with an inner reference electrode (metal/metal oxide) and an outer measuring electrode (Fig. 8a) (e.g., [51, 52, 81, 82, 112–117]). Typical dimensions for commercial tubes are 3–5 cm long and around 5 mm in diameter. The thickness of sensor walls is below or around 1 mm [51, 52, 81, 82].

As mentioned earlier, the oxygen activity might be disturbed close to the sensor walls due to the existence of a small oxide-ion flow established to balance the non-zero electronic current when the sensor is exposed to an oxygen activity gradient. For a sensor wall thickness d , the theoretical current density (J_o) can be expressed as [67, 88, 101, 116]:

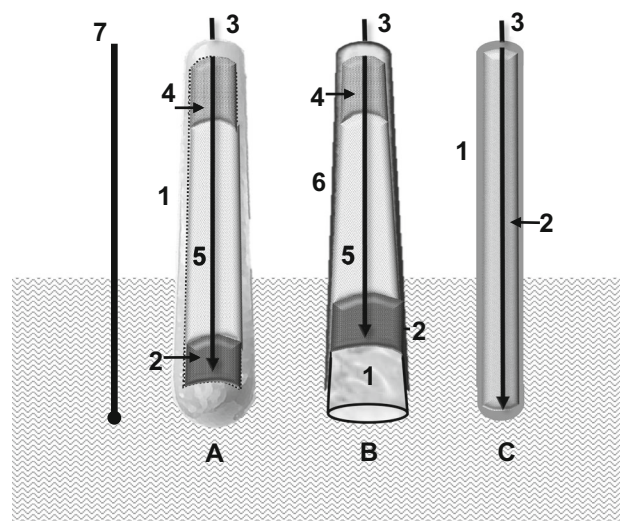


Fig. 8 Schemes of distinct oxygen sensors for molten metals: a closed end tube; b plug-type; c needle-type (I ceramic electrolyte; 2 and 3 reference electrode and electrical contact; 4 seal/cement; 5 inert filler; 6 refractory tube; 7 measuring electrode electrical contact). Drawings not to scale. Adapted from [115]

$$J_o = \frac{\sigma_i(V_o - V)}{d}, \quad (16)$$

where V_o and V are obtained from Eqs. (3) and (8), respectively. Equation (16) shows that the current through the sensor is proportional to $1/d$. Thick sensor walls would be desirable but this is against the economy of a disposable device besides other negative effects, namely time response. Two central parameters related to the electrolyte material that might be used to decrease J_o are σ_i and $P_{(-)}$. The lower the latter value the lower the deviation between V_o and V . The impact of σ_i is direct and obvious.

One solution conceived to circumvent the problem of a thick tube was the plug-type sensor. Here, a cylinder of the sensor material is inserted inside an insulating tube, duly sealed to ensure two isolated chambers (Fig. 8b) [113, 115]. Since the effective thickness of the sensor wall is increased with respect to a conventional tube, the oxidation current within the sensor decreases. Obviously, perfect sealing close to the reference electrode is mandatory.

In line with this type of concern, PSZ sensor tubes were covered with outer layers of distinct electrolyte materials (thin and dense yttria-stabilized zirconia [118] or thick and porous yttria-doped thoria [119]), in order to benefit from the lower electronic conductivity of the outer layer. In this manner the apparent average electronic conductivity of the sensor and $P_{(-)}$ decreased, with inherent improved sensor performance [118, 119].

An alternative design, the usually named needle-type sensor, was introduced to decrease the amount of material needed for each disposable sensor. A metal wire is covered

with layers of the reference electrode and electrolyte material, namely deposited by plasma spraying (Fig. 8c) [114–117]. The sensor diameter is much smaller (1.5–2.5 mm), the concept is simpler (fewer elements), and the time response is shorter, situation obviously interesting for a disposable device. However, with a thinner wall the tendency for electrode polarization is enhanced. Other sensor concepts were also developed to increase the reading accuracy. If one small tip from the sensor material is pressed against the sensor wall the oxide-ion current reaching the most polarizable electrode decreases, decreasing the local oxygen activity disturbance [120].

Designs also addressed issues as distinct as time response or sensor life-time [121–123]. In the first case the sensor wall thickness was changed to assess the impact of this parameter on the response time. Results showed that an ideal range can be identified where oxygen permeation through the sensor tube is kept at low level (favored by a thick sensor wall) while the sensor response time is small enough (favored by a thin sensor wall) [121]. In the second case, two distinct solutions were considered, one based on fabrication parameters, the other on operating conditions. A joint two-step fabrication route for the electrode and electrolyte, using isostatic pressing, yielded a compact body able to sinter progressively during immersion in molten steel, with a life-time of several hours [122]. As alternative, the reference electrode was regenerated with an impressed dc current to supply or remove oxygen to/from the electrode material, depending on the exact sensor working conditions (oxygen activity being measured vs the reference activity). In this manner, the life-time of a sensor could be also extended to several hours [123].

While the most common reference electrodes used in commercial sensors are based on the couples Cr/Cr₂O₃ and Mo/MoO₂, the issue of a proper reference electrode is still under consideration. In general, the electrode should have adequate chemical stability, a well-established oxygen activity, and a significant buffer capacity if operated for long periods of time. Alternative systems studied as reference electrodes included minor additions of other phases to ensure a faster and stable sensor response [124] or more complex phase equilibria including refractory oxides like MgO, Y₂O₃, or rare-earth oxides added to the conventional Cr/Cr₂O₃ couple [125].

6 Electrochemical properties

Considering the wide amount of information being discussed in this section, the corresponding data will be grouped into undoped zirconias and Mg-PSZ related materials.

6.1 Undoped zirconia

The phase transition temperatures in the case of pure zirconia are around 1240 °C for the M to T transformation and around 2370 °C for the T to C transition (Fig. 1). The latter transition is outside the range of conditions of practical interest for oxygen sensors and, to our knowledge, there is no single report on the electrical properties of undoped C zirconia. As a consequence, in this section emphasis will be on the remaining two undoped phases.

Figure 5 and previous comments on impedance spectroscopy introduced some basic information on the electrical performance of m-Zr and t-Zr at low temperature. This was enough to show the clearly distinct conductivity levels exhibited by both phases and also the sharp change in conductivity experienced with the phase transition (Fig. 5b). Figure 4, instead, showed results on the higher temperature isothermal dependence of the conductivity of zirconia on pO₂. The distinct sets of data were selected to highlight common tendencies but also discrepancies. Absolute values from distinct authors may not coincide but tendencies are mostly coherent. The reasons for data mismatch can be found in the previously described experimental techniques (e.g., dc vs constant frequency ac), electrode contacts, undefined purity levels, and microstructural details.

Looking at the pO₂ dependencies, for m-Zr the general shape of all curves includes a conductivity onset for extreme (high and low) pO₂ values. In between the onset of n-type and p-type conductivity, a conductivity plateau. For t-Zr only feeble conductivity changes are noticed for extreme values of pO₂. The overall picture described in these measurements is not far from expectation when performance is governed by acceptor doping, the situation already depicted in Fig. 2.

The estimated slopes of conductivity curves in the mentioned log σ versus log pO₂ plots should also be taken into consideration. Besides the obvious values of (\pm) 1/4 previously discussed, there is also reference to values of 1/5 or 1/6 [70–72, 74–76, 102]. However, mostly for t-Zr, the overall conductivity changes with pO₂ are clearly feeble (Fig. 4) preventing an unequivocal identification of slopes as evidence for distinct defect models (e.g., dominant oxygen vacancies or metal vacancies). Furthermore, reported impurity levels are significant, easily reaching almost 1000 ppm acceptor-type impurities (Ca, Mg, Al, etc.). These arguments justified the assumption in this work of Eq. (4) as model behavior. Data fitting was based on this assumption, with a few examples shown in the inset in Fig. 4. In most cases simple consideration of a constant ionic conductivity contribution and a pO₂ dependent n-type conductivity was enough to obtain quite reasonable fittings under reducing conditions. In fact, p-type conductivity

estimated from high pO_2 data had only a marginal effect on low pO_2 data.

Figure 9a (t-Zr) and 9b (m-Zr) present the results of this fitting procedure for available data sources (Table 1), displayed as Arrhenius-type plots ($\ln \sigma$ vs $1/T$) of ionic (σ_i) and electronic conductivity (σ_n^o) contributions. Naked eye analysis of plots in Fig. 9a shows that absolute values mismatch but their temperature dependencies seem coherent. Also, the higher (slope) activation energy for n-type conductivity is within common expectation for this family of materials.

Data for m-Zr (Fig. 9b) is by far more controversial. The limited number of data sets also preclude any opinion based on a statistical analysis. Somewhat surprisingly, for m-Zr the activation energies for ionic and electronic conductivity are in the same order of magnitude. Considering this reality, and since m-Zr is the least relevant with respect to high temperature sensor performance, further attention will be devoted mostly to t-Zr.

6.2 Doped zirconia

In Mg-PSZ the chemical composition, phase composition, and microstructural characteristics, determining the electrical performance, are deeply interrelated and cannot be completely isolated. Also, published data often provide no details on some of these aspects. Even assuming these limitations, an attempt is made to address separately these three effects before a short reference to other dopants and structures.

6.2.1 Mg-PSZ: role of dopant concentration on conductivity

The main reason to review published data on undoped zirconia was the presumed relevant role of the T phase in Mg-PSZ materials and the up to now neglected relationships between the performance of undoped phases and Mg-PSZ. Since data on the electrical properties of Mg-PSZ are mostly available as listings of $P_{(-)}$ as a function of temperature, data in Fig. 9 were converted to allow a proper comparison between pure zirconia and Mg-PSZ (Fig. 10). A few Mg-PSZ examples were also included for this purpose, ranging from 9 (clearly PSZ) to 15 mol% MgO (close to FSZ). For guidance, the equilibrium pO_2 for the couple Cr/Cr₂O₃ is also included. At higher temperature, this line is in between the sets of data for Mg-PSZ and t-Zr. Considering the physical meaning of $P_{(-)}$, this shows that undoped t-Zr must be a dominant electronic conductor in this temperature range, while Mg-PSZ is a predominant ionic conductor. The enormous shift in performance between t-Zr and m-Zr is highlighted in the figure inset.

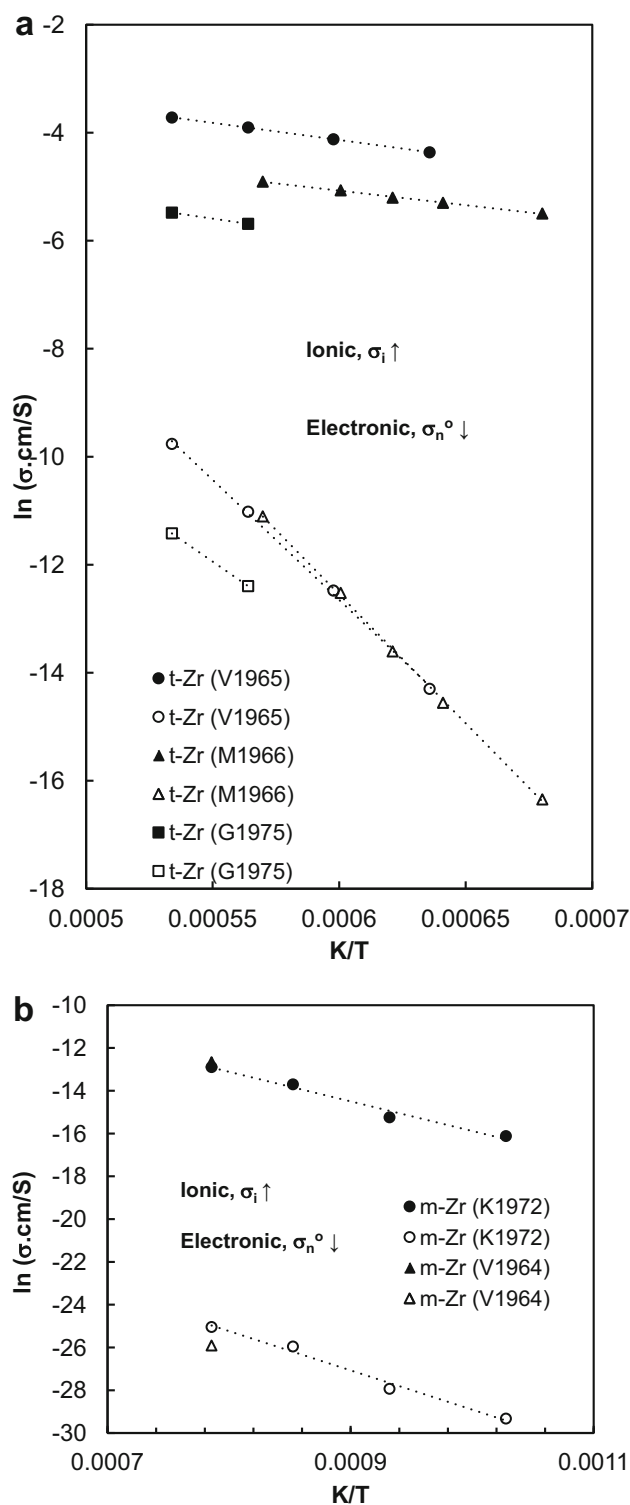


Fig. 9 Arrhenius-type plots of the ionic (σ_i) and electronic (σ_n^o) conductivity as a function of the reciprocal of the absolute temperature ($1/T$), estimated from literature data on the pO_2 and temperature dependencies of the total conductivity of **a** t-Zr and **b** m-Zr. Each vertical pair (filled, open) of symbols corresponds to the fitting results obtained for one temperature. Dashed lines indicate the best fit to the temperature dependencies. Data sources can be found in Table 1

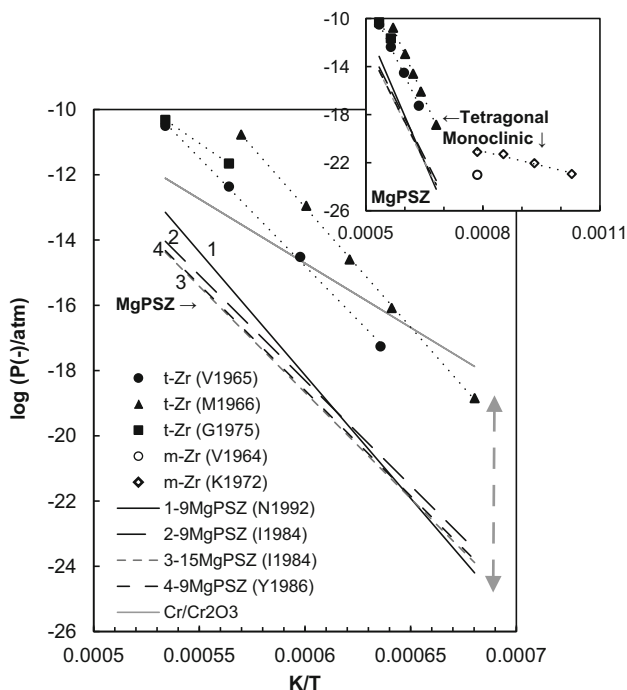


Fig. 10 Published dependence of the $\log P_{(-)}$ on the reciprocal of the absolute temperature ($1/T$) for distinct MgPSZ materials (*lines* only). Estimated data for t-Zr and m-Zr displayed as *symbols* and *dotted lines*. The *inset* details are the relative behavior of m-Zr versus the remaining compositions. Also included the equilibrium pO_2 for the Cr/Cr₂O₃ reference electrode. Data sources can be found in Table 1

In Fig. 10 the clearly aligned performance of t-Zr with respect to Mg-PSZ is quite impressive. To our knowledge this is the first time that this aspect is evidenced. Similar slopes (meaning comparable activation energies and underlying processes) also suggest that the reported properties of undoped t-Zr are in fact governed by impurities. However, this apparent consistency asks for a deeper analysis.

We should recall that $P_{(-)}$ corresponds to the condition where the ionic and n-type conductivity are equal. For a single phase material this implies:

$$[V_{\text{O}}^{\bullet\bullet}] \times \mu_{V_{\text{O}}^{\bullet\bullet}} \times 2e = n \times \mu_e \times e, \tag{17}$$

expressing the ionic and electronic conductivities as a function of the corresponding defect concentration, mobility (μ) and charge. Here the Kroger–Vink notation was adopted to describe the concentrations of oxygen vacancies and electrons ($[V_{\text{O}}^{\bullet\bullet}]$ and n , respectively), while e corresponds to the charge of an electron. For Mg-doped materials, in the extrinsic domain the concentration of dopant ($[Mg_{\text{Zr}}^{\prime\prime}]$) is balanced by the concentration of oxygen vacancies:

$$[V_{\text{O}}^{\bullet\bullet}] = [Mg_{\text{Zr}}^{\prime\prime}]. \tag{18}$$

Also, the relation between the concentration of electrons and oxygen vacancies can be obtained from the equilibrium constant (K_{eq}) of the defect formation reaction (19):



$$K_{\text{eq}} = pO_2^{1/2} \times [V_{\text{O}}^{\bullet\bullet}] \times n^2. \tag{20}$$

Combination of Eqs. (18) and (20) with the condition for $P_{(-)}$ (Eq. (17), or $\sigma_i = \sigma_n$), and consideration of two distinct dopant levels ($[Mg_{\text{Zr},1}^{\prime\prime}]$ and $[Mg_{\text{Zr},2}^{\prime\prime}]$), yields the following relation for the corresponding $P_{(-),i}$ ($i = 1$ or 2) values:

$$P_{(-),2} = \left(\frac{[Mg_{\text{Zr},1}^{\prime\prime}]}{[Mg_{\text{Zr},2}^{\prime\prime}]} \right)^6 \times P_{(-),1}. \tag{21}$$

Equation 21 indicates that $P_{(-)}$ should decrease by 6 orders of magnitude when the dopant content is increased by one order of magnitude. The magnitude of the vertical double arrow inside Fig. 10 corresponds exactly to six orders of magnitude in $P_{(-)}$ and shows that data sets for t-Zr and Mg-PSZ are close to this condition. A significantly lower $P_{(-)}$ for 9MgPSZ with respect to t-Zr can be easily understood since we have certainly more than one order of magnitude difference in the concentration of acceptor cations. We should even expect a larger difference but other arguments might also be invoked to explain this. One example is departure from a dilute defect concentration model behavior, as in most electrolytes when the dopant exceeds a moderate level [126, 127]. However, Eq. (21) is obtained canceling defect mobility terms and equilibrium constants. This should be valid only for one given structure at constant temperature, neglecting the role of defect concentration on mobility. In Mg-PSZ we have two distinct phases and compositions. A somewhat higher ionic conductivity in the T phase could balance a higher electronic conductivity due to a higher concentration of electronic defects [from combination of Eqs. (18) and (20)]. The already mentioned higher conductivity of the T phase (lightly doped) with respect to the C phase (heavily doped) provides some support to these comments.

6.2.2 Mg-PSZ: role of phase content on conductivity

Looking only at chemical composition effects (MgO concentration) without consideration of phase content and composition has obvious limitations. As shown in Fig. 11, in 9MgPSZ the exact MgO content in the T phase is almost constant (around 1 mol%), while in the C phase it is expected to change from about 10–13 mol% on cooling from 1600 to 1400 °C. The relative phase compositions

also change from about 85–65 mol% for the C phase and about 15–35 mol% for the T phase. If the T and C phases were significantly different, we should have a breaking point in such plots when crossing the eutectoid temperature. However, in most reports on $\log P_{(-)}$ versus $1/T$ we find one single slope for the 1200–1600 °C temperature range, as drafted in Fig. 10 for 9MgPSZ.

The previous discussion assumed a condition close to thermodynamic equilibrium above the eutectoid temperature with the Mg-PSZ performance corresponding to a simple mixture of the individual properties of the T and C phases. However, the $C \leftrightarrow T$ transformation process is diffusive and slow at low temperature, and this being the reason why many Mg-PSZ materials possess a significant amount of C phase even at room temperature. Accordingly, an almost monotonous tendency of $P_{(-)}$ with the temperature might simply indicate significant deviation from equilibrium. In fact, most measurements must be performed in a short period of time considering the demanding experimental conditions. In such circumstances the conversion $C \rightarrow T$ might be incomplete, with the phase composition almost frozen throughout measurements.

As a complement to this discussion, a few reports indeed noticed likely transient conditions involved in typical $P_{(-)}$ measurements or suggested distinct slopes within this

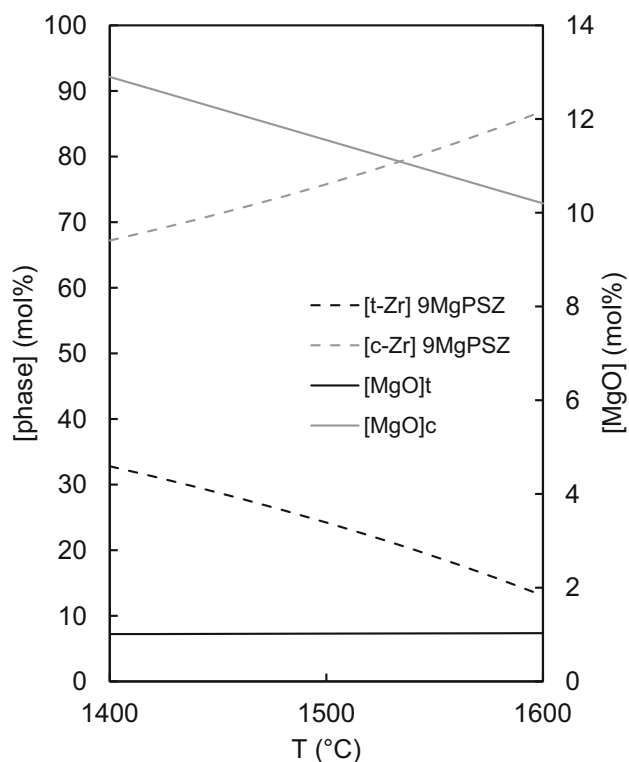


Fig. 11 Estimated equilibrium concentrations of C (c-Zr) and T (t-Zr) zirconia in 9MgPSZ and corresponding MgO content ([MgO]) within the 1400–1600 °C temperature range (derived from Fig. 1)

temperature range [54, 81, 83]. One of such examples is detailed in the inset in Fig. 12, including additional data sets. Here, a range of $P_{(-)}$ values is suggested for two materials. For temperatures below the eutectoid, $P_{(-)}$ values exceed those resulting from the higher temperature tendency. This indicates that either the ionic conductivity tends to be lower or the n-type conductivity tends to be higher. Even so, the overall differences are small.

The relative magnitude of the conductivity of the T and C phases was also addressed several times in the literature, in all cases with claims that the conductivity of the T phase was higher, as previously noticed (see Sect. 4.2). Interestingly, these claims include data obtained from relatively low temperatures up to 1450 °C [73, 77, 80, 86]. Figure 13 shows two examples of conductivity data obtained for Mg-PSZ as a function of temperature [77]. For 4.7MgPSZ, two step-like changes can be found on heating or cooling. This material is close to the T single phase field which means that the T phase should be always dominant within the high temperature range. On the contrary, for 11.4MgPSZ the C phase should be dominant. Data shows that the higher conductivity is observed for the lower dopant content material, richer in T phase. The confirmation of the

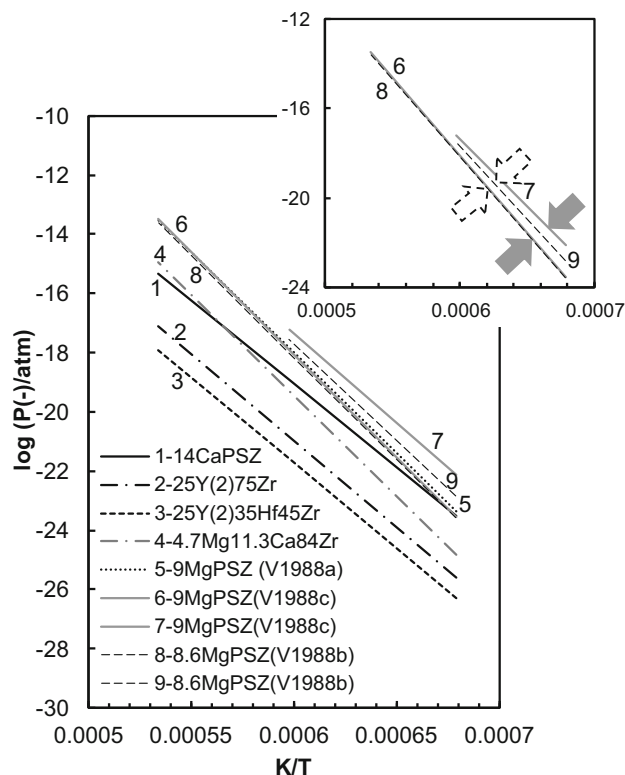


Fig. 12 Published dependence of the $\log P_{(-)}$ on the reciprocal of the absolute temperature ($1/T$) for distinct electrolyte materials with dominant cubic zirconia. The inset details are the range of values reported for temperatures below the eutectoid (for 9MgPSZ). Data sources can be found in Table 1

relevance of the T phase in both materials can also be obtained from distinct conductivity steps with temperature. Almost no hysteresis for the higher C phase content but a large step-like change coinciding with the M ↔ T phase transitions in the lightly doped material.

Looking at the isothermal dependence of conductivity on composition (Fig. 13, inset), the trend is confirmed. Extreme compositions show similar conductivity levels, with some benefit for materials with lower dopant content. The conductivity dependence on dopant concentration is by no means linear, emphasizing that the dilute defect concentration model is not valid.

6.2.3 Mg-PSZ: role of microstructural effects on conductivity

Figure 10 showed that the performance of 15MgPSZ is hardly distinguished from 9MgPSZ. This is somewhat

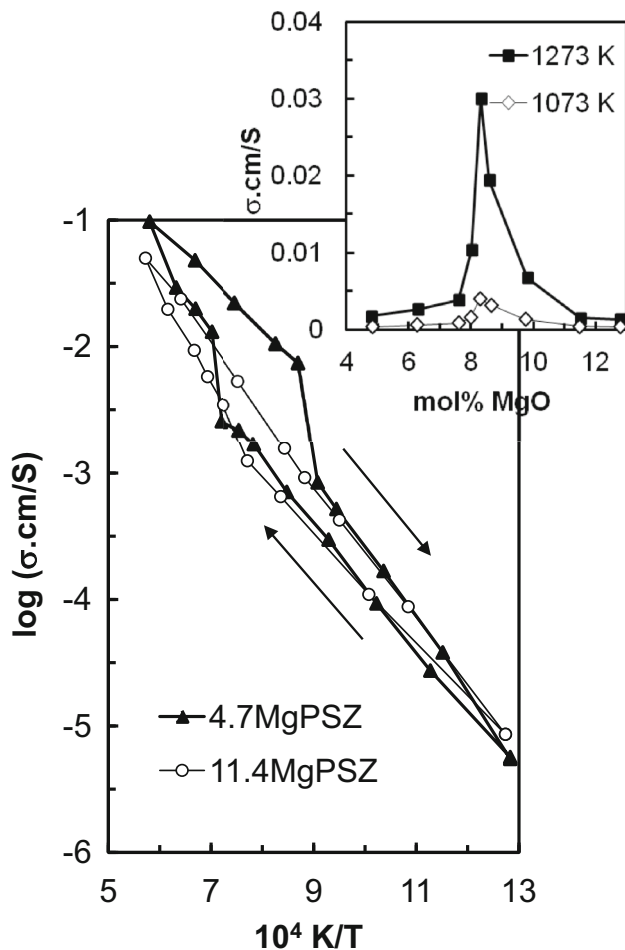


Fig. 13 Data on the published dependence of the log σ on the reciprocal of the absolute temperature ($1/T$) for distinct MgPSZ materials (arrows indicate the temperature sequence of measurements). The inset details are the isothermal conductivity dependence on temperature. Adapted from [77]

surprising considering the distinct dopant levels, phase composition, and isothermal conductivity plots where maximum conductivity values were obtained for intermediate compositions, appearing as well localized peaks. The usual smooth maximum conductivity dependence on dopant content observed in many fluorite-type electrolytes is not observed here [126, 127]. The conductivity increases by almost an order of magnitude, while the dopant concentration increases by a factor of only 2, followed by an equally sharp decrease. This situation, far from trivial, recommends some attention to possible microstructural effects.

As first remark, we have no clear indication on the porosity of most samples. However, MgO-doped samples usually have higher densification than undoped materials [73]. This means that any likely advantage in conductivity with respect to densification should be found for materials closer to the C phase field. Densification is hardly a critical issue.

On the contrary, we should recall that typical Mg-PSZ microstructures include large C grains often surrounded by M regions. The C grains are also populated with ellipsoidal precipitates of the T and/or M phases, as depicted in Fig. 14 (e.g., [11, 14, 24]). Most of these precipitates are formed on cooling. Furthermore, the thermal expansion coefficient of the T phase is lower than that of the C phase [128]. This means that defective and strained interface/interphase regions may be immense in these materials. These regions might offer favorable ionic pathways, in line with recent findings involving dislocations or heterostructures [129–131].

For low-dopant concentrations (<5 mol% MgO), the C phase grains are dispersed, hardly percolating. For large-dopant concentrations (10–15 mol% MgO), the C phase grains dominate and the T/M phases tend to vanish. Intermediate dopant contents provide the required unique microstructural characteristics where strained regions might percolate, offering ideal ionic pathways. This could explain the peak type dependence of conductivity on dopant concentration reported for these materials. This kind of composite effect would deviate the material performance from simple expectation based on direct compositional effects or a mixture of properties of constituent phases. This effect might be preserved on cooling since phase changes are slow. This could explain the relatively good performance of 9MgPSZ with respect to 15MgPSZ.

In summary, considering exclusively published data, we can suggest plausible reasons for the parallel performance of t-Zr and Mg-PSZ, for the almost indiscernible behavior of 9MgPSZ versus 15MgPSZ, and for the reported linear dependence of log $P_{(-)}$ versus $1/T$. We can also speculate on the reasons for the unusual peak type conductivity dependence on composition. However, we must recall that

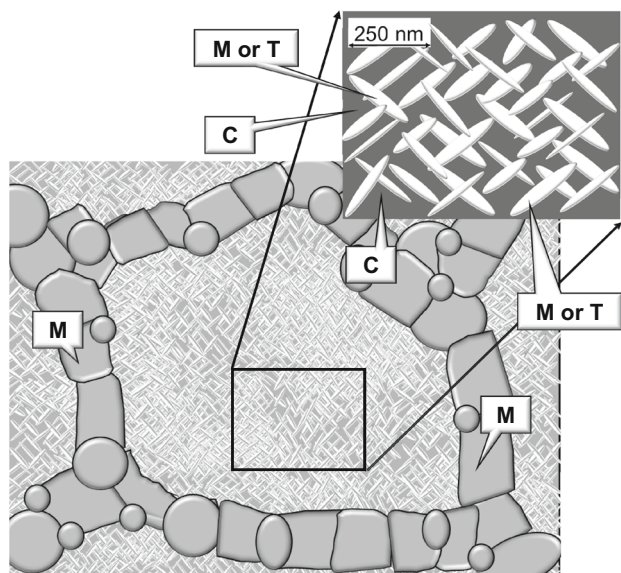


Fig. 14 Scheme of a typical microstructure of Mg-PSZ with dispersed elongated T or M phase particles (white) within large C grains. Also present are M regions in between C grains Adapted from [24, 47]

distinct effects besides chemical composition are certainly influential. Without a clear knowledge of actual phase composition, porosity and other microstructural characteristics of all materials, comparative analysis between distinct sets of data has obvious limitations. The possibility of mismatching characteristics of materials with similar chemical compositions should be always present. As example, at 500 °C the conductivity dependence on dopant content showed a continuous enhancement between 3.2MgPSZ and 13.7MgPSZ [73], unlike reported in [77]. Even so, the conductivity of heavily doped samples exceeded by far what might be expected from a simple defect concentration effect, with a two-fold dopant increase (6.8–13.7 mol% MgO) being responsible for one order of magnitude conductivity enhancement [73]. In this work, prolonged thermal treatments (800 °C, 15 h) while curing the metal electrodes, promoted a high conversion of T (conducting) into M (insulating) phase, the latter often exceeding 50 vol%. These aspects should be kept in mind, since they really prevent a direct comparison between these sets of data.

6.2.4 Other dopants and structures

For the analysis of other systems besides Mg-PSZ, Fig. 12 should be considered again. CaO and Y₂O₃ are slightly more effective than MgO to lower the higher temperature values of $P_{(-)}$. This might be due to the higher ionic conductivity of Ca-PSZ when compared to Mg-PSZ (see

Table 2). Materials with a large Y content also show a rather positive performance mostly at high temperature, with $P_{(-)}$ values up to 4 orders of magnitude lower than those reported for Mg-PSZ (Table 3). This explains the previously mentioned introduction of sensor concepts including YSZ coatings.

The high Y content under consideration (25 mol%) exceeds the usual level for maximum oxide-ion conductivity in YSZ, close to 8 mol%. This might indicate that the beneficial effect in $P_{(-)}$ is due mainly to a decreasing concentration of electronic defects and corresponding conductivity rather than an enhanced ionic conductivity. In fact, the dependence of n on dopant concentration can be obtained again combining the electroneutrality condition ($2 \cdot [V_{O}^{\bullet}] = [Y'_{Zr}]$) with the definition of K_{eq} (Eq. 20), yielding, at constant pO_2 :

$$n_2 = \left(\frac{[Y'_{Zr,1}]}{[Y'_{Zr,2}]} \right)^{1/2} \times n_1, \quad (22)$$

where the subscripts 1 and 2 indicate two distinct dopant levels. This means that the higher the dopant content the lower the concentration of electronic defects. The relevance of this fact is emphasized considering the reported superior ionic conductivity of 9MgPSZ with respect to 8Y(2)92Zr at high temperature (>1300 °C), due to a higher activation energy [97].

Figure 15 includes one final set of compositions also tested as sensor electrolytes. HfO₂-based (fluorite) and ThO₂-based (fluorite) materials in general show a positive performance with respect to Mg-PSZ in the entire temperature range, situation mostly evident looking at the listing in Table 3. This explains again the utilization of ThO₂-based coatings to improve the performance of Mg-PSZ sensors. The HfO₂ and Gd₂O₃-based pyrochlore shows no obvious benefit with respect to the remaining hafnia-based materials. CaZrO₃-based (perovskite) materials are interesting examples where a modest ionic conductivity combined with an even more modest electronic conductivity yields some of the lowest $P_{(-)}$ values found in the literature.

The above results show that there is no special trend with respect to structure but host oxides based on group VIB, other than ZrO₂, tend to have lower $P_{(-)}$ values. Table 3 also shows that the ionic domains of all materials considered in this work are constrained, none of them reaching a comfortable level to ensure ideal sensor performance at high temperature and under reducing conditions. Thus, materials selection must rely on other aspects, namely the thermomechanical performance, since thermal shock is obviously a main issue in sensor performance.

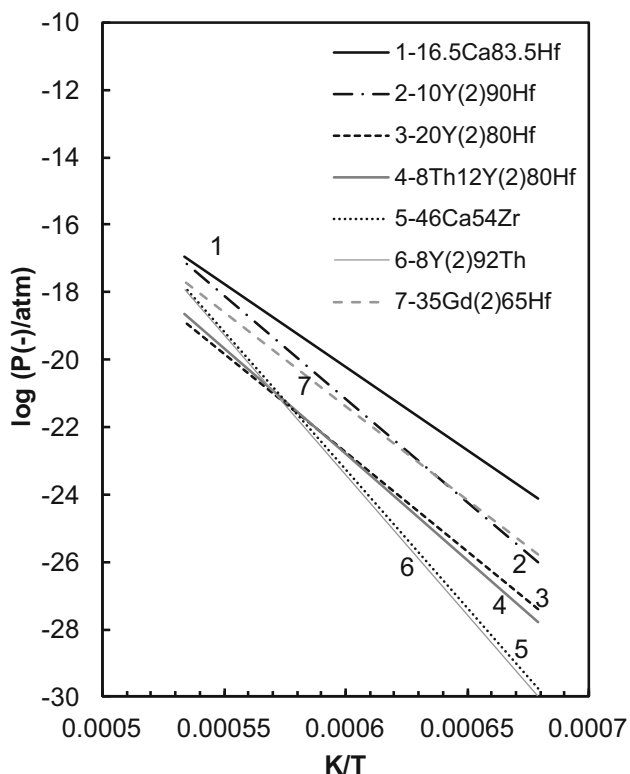


Fig. 15 Published dependence of the $\log P_{(-)}$ on the reciprocal of the absolute temperature ($1/T$) for distinct electrolyte materials with diverse compositions and structures. Data sources can be found in Table 1

7 Concluding remarks

Previous disputes on the defect chemistry of pure zirconia were mostly based on feeble pO_2 conductivity dependencies [70–72, 74–76]. To the best of our knowledge there was only one previous attempt to relate the performance of undoped and doped zirconias, situation achieved using a small concentration of Y_2O_3 as dopant (1.4 mol%) and preserving a small grain size [93], based on total conductivity measurements in air, where the p-type conductivity of undoped Zr cannot be neglected. Even so, the conductivity of the lightly yttria-doped zirconia was clearly between the values reported for undoped zirconia and YSZ, suggesting a smooth transition in performance governed by defect concentration either due to doping or impurities.

The present analysis of $P_{(-)}$ values has a few advantages to comment on defect chemistry. Firstly, a wide grouping of data from distinct authors provide adequate screening of possible experimental constraints. Secondly, microstructural effects (porosity, cracks) or ineffective electrode contacts should cancel when dealing with $P_{(-)}$. As an example, porosity is expected to influence in a similar manner the ionic and the electronic conductivity, while absolute conductivity readings are sensitive to this aspect.

Higher $P_{(-)}$ values hereby determined for t-Zr were obtained with samples with Fe as significant impurity (Table 1; [76]). Transition metals are known to increase the electronic conductivity of solid electrolytes [132–134]. On the contrary, the t-Zr sample with lower $P_{(-)}$ values had a reported content in Ca and Mg in the order of 400 ppm (Table 1; [74]). These impurities are expected to play exclusively the role of acceptor dopants, as in Mg- or Ca-PSZ. Overall, the parallel trends observed for the $P_{(-)}$ values of t-Zr and Mg-PSZ and the relative values within the t-Zr sets of data seem to indicate that impurities really determined the performance of the so-called undoped materials.

As mentioned, published literature on these materials provides conflicting information on their defect chemistry. Previous comments showed that the hereby assumed model can be used to explain most observations in a coherent manner. However, there is a clear need to inspect again these materials using tailored experimental conditions.

Data on Mg-PSZ and related systems show a significant level of inconsistencies besides those already discussed. $P_{(-)}$ values at 1600 °C for materials with the same nominal composition (e.g., 9MgPSZ) range from 7.1×10^{-14} [69] to 9.1×10^{-15} [81]. Activation energies for ionic conduction move from 1.25 to 0.68 eV for close compositions (12CaPSZ vs 13CaPSZ, see [67, 88], respectively). Lacking details might explain such results. As previously mentioned, these materials are likely to shift in phase composition and microstructure with elapsed time during measurements. Even so, Mg-PSZ might hide yet undisclosed features involving ionic transport via phase boundaries. Unusual trends in conductivity with respect to composition suggest the uniqueness of this material with respect to other zirconia or fluorite-type oxide structures. Mg-PSZ microstructures are unique with respect to common electrolyte materials. All these issues suggest again the need to reassess the performance of these materials.

Ceramic electrolytes for oxygen sensors are asked to combine demanding electrical and thermomechanical properties to provide an accurate reading in only a few seconds, after sudden immersion in molten steel. To meet the first requirement, these ceramics must possess a large ionic domain, desirably extending to pO_2 values as low as 10^{-20} atm, to obey ideal performance up to 1600 °C. Figure 16 shows typical sensor readings as a function of the oxygen activity in molten steel (expressed in ppm, typical unit widely adopted in this field). Data from 9MgPSZ [81] was combined with information on the relations between pO_2 and oxygen activity in molten steel [135]. Sensor materials deviate seriously from ideal performance in the low ppm range (<1 ppm). Since distinct materials deviate distinctly from ideal performance, this

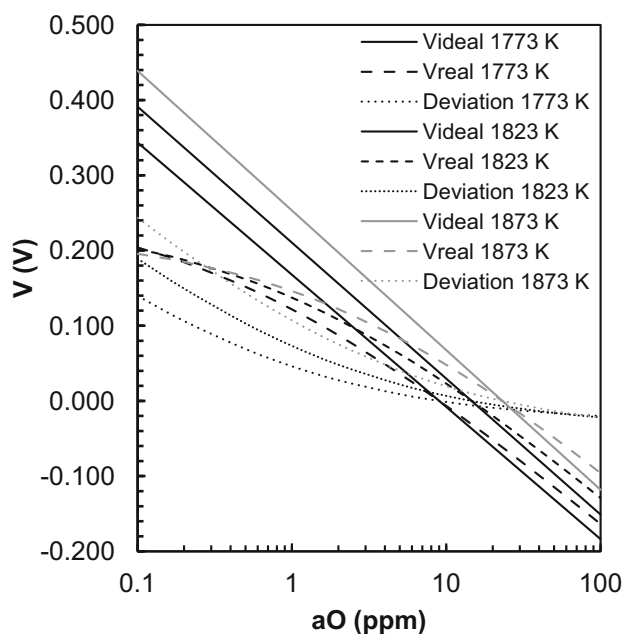


Fig. 16 Estimated dependence of the actual sensor voltage reading and ideal values (V) for 9MgPSZ [81], as a function of the oxygen activity (aO) in molten steel, using a Cr/Cr_2O_3 reference electrode, in the temperature range 1773–1873 K. Further details can be found in the main text

situation can easily be the source of problems when inadequate calibration curves are used.

To reach a reading, sensors should survive to thermal shock. This capability is enhanced with an adequate sintering profile or thermal treatment after sintering, to obtain a desirable balance in the proportions of all phases (M, T and C) but also the required microstructure. Dispersed nanosized T precipitates within C grains are the basis of the toughening effect in PSZ materials. Finely dispersed M precipitates within C grains can be used to adjust the thermal expansion behavior of PSZ materials. The efficacy of thermal treatments to obtain enhanced thermomechanical properties is widely detailed in the literature, including specific examples addressing the case of oxygen sensors [136, 137]. This requirement explains why other studied materials with wider ionic domains fail with respect to this specific application.

Acknowledgements This work was funded by CICECO - Aveiro Institute of Materials (Ref. FCT UID/CTM/50011/2013), financed by national funds through FCT/MEC and when applicable co-financed by FEDER under the PT2020 Partnership Agreement. Research grants from FCT, Portugal (A. Rondão, SFRH/BDE/52139/2013), and CNPq (454275/2016-1) and FAPESP (2016/20708-6 and 2013/07296-2), Brazil, are also highly appreciated.

References

- Gulati S, Helfinstine J, Davis A (1980) Determination of some useful properties of partially stabilized zirconia and the application to extrusion dies. *Am Ceram Soc Bull* 59:211–212
- Lamon J, Thorel A, Broussaud D (1986) Influence of long-term ageing upon the mechanical properties of partially stabilized zirconia (Mg-PSZ) for heat-engine applications. *J Mater Sci* 21:2277–2282
- Kara A, Tobyn MJ, Stevens R (2004) An application for zirconia as a pharmaceutical die set. *J Eur Ceram Soc* 24:3091–3101
- Al-Amleh B, Lyons K, Swain M (2010) Clinical trials in zirconia: a systematic review. *J Oral Rehabil* 37:641–652
- Heintze SD, Rousson V (2010) Survival of zirconia- and metal-supported fixed dental prostheses: a systematic review. *Int J Prosthodont* 23:493–502
- Lughi V, Sergio V (2010) Low temperature degradation -aging- of zirconia: a critical review of the relevant aspects in dentistry. *Dent Mater* 26:807–820
- Garvie RC, Nicholson PS (1972) Structure and thermomechanical properties of partially stabilized zirconia in the $CaO-ZrO_2$ system. *J Am Ceram Soc* 55:152–157
- Porter DL, Heuer AH (1977) Mechanisms of toughening partially stabilized zirconia (PSZ). *J Am Ceram Soc* 60:183–184
- Gupta TK, Bechtold JH, Kuznicki RC et al (1977) Stabilization of tetragonal phase in polycrystalline zirconia. *J Mater Sci* 12:2421–2426
- Hannink RHJ (1978) Growth morphology of the tetragonal phase in partially stabilized zirconia. *J Mater Sci* 13:2487–2496
- Porter DL, Heuer AH (1979) Microstructural development in MgO-partially stabilized zirconia (Mg-PSZ). *J Am Ceram Soc* 62:298–305
- Kobayashi K, Kuwajima H, Masaki T (1981) Phase change and mechanical properties of $ZrO_2-Y_2O_3$ solid electrolyte after ageing. *Solid State Ionics* 3–4:489–493
- Hannink RHJ, Garvie RC (1982) Sub-eutectoid aged Mg-PSZ alloy with enhanced thermal up-shock resistance. *J Mater Sci* 17:2637–2643
- Hannink RHJ (1983) Microstructural development of sub-eutectoid aged MgO- ZrO_2 alloys. *J Mater Sci* 18:457–470
- Hannink RHJ, Murray MJ, Scott HG (1984) Friction and wear of partially stabilized zirconia: basic science and practical applications. *Wear* 100:355–366
- Chaim R, Brandon DG (1984) Microstructure evolution and ordering in commercial Mg-PSZ. *J Mater Sci* 19:2934–2942
- Garvie RC, Swain MV (1985) Thermodynamics of the tetragonal to monoclinic phase transformation in constrained zirconia microcrystals, Part 1 In the absence of an applied stress field. *J Mater Sci* 20:1193–1200
- Sato T, Ohtaki S, Shimada M (1985) Transformation of yttria partially stabilized zirconia by low-temperature annealing in air. *J Mater Sci* 20:1466–1470
- Evans AG, Cannon RM (1986) Toughening of brittle solids by martensitic transformations. *Acta Metall* 34:761–800
- Echigoya J, Sasai K, Suto H (1988) Microstructural change of 11 mol% MgO- ZrO_2 by aging. *Trans Jpn Inst Met* 29:561–569
- Wu F, Yu S (1988) The effect of β -phase, $Mg_2Zr_5O_{12}$, on the stabilizations of the tetragonal phase in Mg-PSZ. *Mater Res Bull* 23:467–474
- Christel P, Meunier A, Heller M et al (1989) Mechanical properties and short-term in vivo evaluation of yttrium-oxide-partially-stabilized zirconia. *J Biomed Mater Res* 23:45–61
- Okada H, Tamura T, Ramakrishnan N et al (1992) Analysis of toughening of magnesia partially stabilized zirconia, due to dilatation transformation. *Acta Metall Mater* 40:1421–1432
- Hannink RHJ, Kelly PM, Muddle BC (2000) Transformation toughening in zirconia-containing ceramics. *J Am Ceram Soc* 87:461–487
- Chevalier J, Gremillard L, Virkar AV, Clarke DR (2009) The tetragonal-monoclinic transformation in zirconia: lessons learned and future trends. *J Am Ceram Soc* 92:1901–1920

26. Hannink RHJ, Stringer RK, Swain MV (2014) The development of zirconia transformation toughened ceramics in Australia. *J Aust Ceram Soc* 50:1–14
27. Jiang L, Guo S, Qiao M et al (2017) Study on the structure and mechanical properties of magnesia partially stabilized zirconia during cyclic heating and cooling. *Mater Lett* 194:26–29
28. Jacobson NS (1989) Thermodynamic properties of some metal oxide-zirconia systems. NASA Tech Memo 102351:1–64
29. Duwez P, Odell F, Brown FH (1952) Stabilization of zirconia with calcia and magnesia. *J Am Ceram Soc* 35:107–113
30. Grain CF (1967) Phase relations in the ZrO_2 - MgO system. *J Am Ceram Soc* 50:288–290
31. Scott HG (1975) Phase relationships in the zirconia-yttria system. *J Mater Sci* 10:1527–1535
32. Farmer SC, Heuer AH, Hannink RHJ (1987) Eutectoid decomposition of MgO -partially-stabilized ZrO_2 . *J Am Ceram Soc* 70:431–440
33. Stubican VS, Hellman JR (1981) Phase equilibria in some zirconia systems. Science and technology of zirconia. In: Heuer AH, Hobbs LW (eds) *Advanced ceramics*. American Ceramic Society, Columbus, pp 25–36
34. Dickerson RM, Heuer AH (1991) The calcia-zirconia phase diagram revisited: stability of the ordered phases φ_1 and φ_2 . *J Am Ceram Soc* 74:234–237
35. Viechnicki D, Stubican VS (1965) Mechanism of decomposition of the cubic solid solutions in the system ZrO_2 - MgO . *J Am Ceram Soc* 48:292–297
36. Viechnicki D, Stubican VS (1965) Phase studies within the system ZrO_2 - MgO . *Lett to Nature*. *Nature* 206:1251–1252
37. Sim SM, Stubican VS (1987) Phase relations and ordering in the system ZrO_2 - MgO . *J Am Ceram Soc* 70:521–526
38. Farmer SC, Schoenlein LH, Heuer AH (1983) Precipitation of $Mg_2Zr_5O_{12}$ in MgO -partially-stabilized ZrO_2 . *Commun Am Ceram Soc* 66:C107–C109
39. Stubican VS (1986) Phase equilibria and metastabilities in the systems ZrO_2 - MgO , ZrO_2 - CaO and ZrO_2 - Y_2O_3 . *Adv Ceram* 24:71–82
40. Duran P, Rodriguez JM, Recio P (1991) The ZrO_2 -rich region of the ZrO_2 - MgO system. *J Mater Sci* 26:467–472
41. Du Y, Jin Z (1991) Optimization and calculation of the ZrO_2 - MgO system. *Calphad* 15:59–68
42. Fitterer GR (1973) Means for determining the oxygen. US Patent 3773641 A
43. Tanaka K, Saito T, Suzuki M, Ouki M (1982) Solid electrolyte for use in oxygen concentration sensor. US Patent 4328294 A
44. Worrell WL, Liu Q-G (1986) Electrochemical sensors and methods for their manufacture and use. US Patent 4627892
45. Merckens W, Schmitz N (2009) Probe for determination of oxygen activity in metal melts and methods for its production. US Patent 7578913 B2
46. Villarreal V AZ, Turner PA (2014) Immersible oxygen sensor for molten metals. US Patent 8689650 B2
47. Garvie RC, Hannink RHJ, McKinnon NA (1980) Partially stabilized zirconia ceramics; method of making said ceramics, dies constructed of said ceramics, cutting tools with a cutting surface and tappet facings formed of said ceramics. Eur Patent 0013599:B1
48. Yamada K, Shinya Y (1982) Sintering method of zirconia. US Patent 4344904 A
49. Bush EA, Reddy KP, Socha LS (1989) Magnesia partially-stabilized zirconia. US Patent 4835123 A
50. Chatterjee DK, Majumbar D, Ghosh SK, Mir JM (1994) Zirconia ceramic articles having a tetragonal core and cubic casing. US Patent 5358913 A
51. Nakamura H, Mariya T (1983) Study on solid electrolyte for oxygen activity measurements in steelmaking process. *Solid State Ionics* 9 & 10:1257–1262
52. Yamada K, Shinya Y, Tanaka K (1981) Properties of oxygen sensors for steelmaking. *Solid State Ionics* 3–4:595–598
53. Van Wijngaarden MJUT, Dippenaar RJ, Van Den Heever PM (1987) An evaluation of the electrochemical oxygen probes used in steelmaking. *J S Afr Inst Min Metall* 87:269–278
54. Van Wijngaarden MJUT, Geldenhuis JMA, Dippenaar RJ (1988) A quantitative assessment of mixed ionic and electronic conduction in some commercially available magnesia-stabilized zirconia electrolytes. *ISS Trans* 4:35–44
55. Weppner W (1992) Tetragonal zirconia polycrystals—a high performance solid oxygen ion conductor. *Solid State Ionics* 52:15–21
56. Bonanos N, Slotwinski RK, Steele BCH, Butler EP (1984) High ionic conductivity in polycrystalline tetragonal Y_2O_3 - ZrO_2 . *J Mater Sci Lett* 3:245–248
57. Minh NQ (1993) Ceramic fuel cells. *J Am Ceram Soc* 76:563–588
58. Kharton VV, Marques FMB, Atkinson A (2004) Transport properties of solid oxide electrolyte ceramics: a brief review. *Solid State Ionics* 174:135–149
59. Stambouli AB, Traversa E (2002) Solid oxide fuel cells (SOFCs): a review of an environmentally clean a deficient source of energy. *Renew Sustain Energy Rev* 6:433–455
60. Laguna-Bercero MA (2012) Recent advances in high temperature electrolysis using solid oxide fuel cells: a review. *J Power Sources* 203:4–16
61. Liu T, Zhang X, Wang X et al (2016) A review of zirconia-based solid electrolytes. *Ionics (Kiel)* 22:2249–2262
62. Möbius H-H (1992) Solid-state electrochemical potentiometric sensors for gas analysis. In: Gopel W, Hesse J, Zemel JN (eds) *Sensors, a comprehensive survey*. Wiley, Weinheim, pp 1104–1154
63. Fouletier J, Mantel E, Kleitz M (1982) Performance characteristics of conventional oxygen gauges. *Solid State Ionics* 6:1–13
64. Fouletier J, Henault M (1983) Doped ceria electrolyte in oxygen sensors. *Solid State Ionics* 9–10:1277–1281
65. Wirtz GP, Marques FMB (1992) Oxygen fugacity control in nonflowing atmospheres: II, theoretical model. *J Am Ceram Soc* 75:375–381
66. Marques FMB (2000) On the accuracy of oxygen pressure measurements. *Ionics (Kiel)* 6:22–29
67. Janke D, Richter H (1979) Low oxygen activities in steel melts—possibilities and limits of the solid electrolyte measuring technique. *Arch für das Eisenhüttenwes* 50:93–100
68. Iwase M, McLean A (1981) Evaluation of electrochemical oxygen probes for use in steelmaking. *Solid State Ionics* 5:571–574
69. Nagatani A, Inoue R, Suito H (1992) Determination of electronic conductivity limits of mullite and ZrO_2 -9 mol% MgO solid electrolytes. *J Appl Electrochem* 22:859–864
70. Kofstad P, Ruzicka DJ (1963) On the defect structure of ZrO_2 and HfO_2 . *J Electrochem Soc* 110:181–184
71. Vest RW, Tallan N, Tripp WC (1964) Electrical properties and defect structure of zirconia. *J Am Ceram Soc* 47:635–640
72. Kumar A, Rajdev D, Douglass DL (1972) Effect of oxide defect structure on the electrical properties of ZrO_2 . *J Am Ceram Soc* 55:439–445
73. Muccillo ENS, Kleitz M (1996) Impedance spectroscopy of Mg-partially stabilized zirconia and cubic phase decomposition. *J Eur Ceram Soc* 16:453–565

74. Vest RW, Tallan NM (1965) Electrical properties and defect structure of zirconia: II, tetragonal phase and inversion. *J Am Ceram Soc* 48:472–475
75. McClaine LA, Coppel CP (1966) Electrical conductivity studies of tetragonal zirconia. *J Electrochem Soc* 113:80–85
76. Guillot A, Anthony AM (1975) Interprétation de la conductivité électrique de ZrO_2 et de HfO_2 à haute température (1300°C–1600°C). *J Solid State Chem* 15:89–95
77. Tinglian W, Xiaofei L, Chukun K, Weppner W (1986) Conductivity of MgO-doped ZrO_2 . *Solid State Ionics* 18 & 19:715–719
78. Fischer WA, Janke D (1976) Effect of carbon, silicon, aluminium, or titanium on the oxygen activity in alloyed steel melts. *Arch für das Eisenhüttenwes* 47:589–594
79. Janke D, Fischer WA (1977) Electrical properties of solid oxide electrolytes at steelmaking temperatures. *Arch für das Eisenhüttenwes* 48:311–318
80. Muccillo R, Muccillo ENS, Saito NH (1998) Thermal shock behavior of ZrO_2 :MgO solid electrolytes. *Mater Lett* 34:128–132
81. Iwase M, Ichise E, Takeuchi M, Yamasaki T (1984) Measurements of the parameters, P_{-} , for determinations of mixed ionic and n-type electronic conduction in commercial zirconia electrolytes. *Trans Jpn Inst Met* 25:43–52
82. Yamada K, Murase M, Iwase M (1986) Determination of mixed ionic and electronic conduction in commercial-grade magnesia-stabilized zirconia electrolyte. *J Appl Electrochem* 16:712–718
83. Van Wijngaarden MJUT, Geldenhuis JMA, Dippenaar RJ (1988) An experimental technique employing a high-temperature gas-tight alumina seal for the assessment of the electrical properties of solid electrolytes. *J Appl Electrochem* 18:724–730
84. Muccillo R, Saito NH, Muccillo ENS (1995) Properties of zirconia-magnesia solid electrolytes prepared by the citrate method. *Mater Lett* 25:165–169
85. Muccillo ENS, Kleitz M (1995) Ionic conductivity of fully stabilized ZrO_2 : MgO and blocking effects. *J Eur Ceram Soc* 15:51–55
86. Bonanos N, Slotwinski RK, Steele BCH, Butler EP (1984) Electrical conductivity/microstructural relationships in aged CaO and CaO + MgO partially-stabilized zirconia. *J Mater Sci* 19:785–793
87. Inouye M, Iwase M, Mori T (1981) Mixed ionic and n-type electronic conduction in commercial ZrO_2 + CaO electrolyte. *Trans ISIJ* 21:54–55
88. Iwase M, Mori T (1978) Oxygen permeability of calcia-stabilized zirconia at low oxygen partial pressures. *Metall Trans B* 9B:653–656
89. Dudek M (2008) Composite oxide electrolytes for electrochemical devices. *Adv Mater Sci* 8:15–30
90. Weyl A, Janke D (1997) High-temperature ionic conduction in multicomponent solid oxide solutions based on zirconia. *J Am Ceram Soc*, p 73
91. Tien TY (1964) Electrical conductivity in the system ZrO_2 - $CaZrO_3$. *J Am Ceram Soc* 47:430–433
92. Janke D (1982) Oxygen probes based on calcia-doped hafnia or calcium zirconate for use in metallic melts. *Metall Trans B* 13B:227–235
93. Gupta TK, Grekila RB (1981) Electrical conductivity of tetragonal zirconia below the transformation temperature. *J Electrochem Soc* 44:929–931
94. Janke D (1978) Electrolytic deoxidation of iron melts. *Arch für das Eisenhüttenwes* 49:217–224
95. Weyl A, Janke D (1996) High-temperature ionic conduction in multicomponent solid oxide solutions based on HfO_2 . *J Am Ceram Soc* 79:2145–2155
96. Hufschmidt H, Weyl A, Janke D (1996) High-temperature electrical properties in the ThO_2 -rich region of ThO_2 - RE_2O_3 systems. *J Am Ceram Soc* 79:756–762
97. Yoon S, Noh T, Kim W et al (2013) Structural parameters and oxygen ion conductivity of Y_2O_3 - ZrO_2 and MgO - ZrO_2 at high temperature. *Ceram Int* 39:9247–9251
98. Schmalzried H (1963) Ionen- und elektronenleitung in binären oxiden und ihre untersuchung mittels EMK-Messungen. *Zeitschrift für Phys Chemie* 102:87–102
99. Kroger FA (1966) Electronic conductivity of calcia-stabilized zirconia. *J Am Ceram Soc* 49:215–218
100. Tuller HL (1981) Non-stoichiometric oxides. Academic Press, New York
101. Marques RMC, Marques FMB, Frade JR (1994) Characterization of mixed conductors by dc techniques. Part I: theoretical solutions. *Solid State Ionics* 73:15–25
102. Kofstad P (1972) Nonstoichiometry, diffusion and electrical conductivity in binary metal oxides. Wiley-Interscience, New York
103. Mazandarany FN, Pehlke RD (1974) Standard free energy of formation of Cr_2O_3 . *J Electrochem Soc* 121:711–714
104. Kawakami M, Goto KS, Matsuoka M (1980) A solid electrolyte oxygen sensor for steelmaking slags of the basic oxygen converter. *Metall Trans B* 11:463–469
105. Bauerle JE (1969) Study of solid electrolyte by a complex admittance method. *J Phys Chem Solids* 30:2657–2670
106. An S, Wu W, Liu Q (1988) Measurement of electronic conductivity and phase ratio for MgO partially stabilized zirconia. *Solid State Ionics* 28–30:546–549
107. An S, Zhou T, Wu W, Liu Q (1990) Investigation of electronic conductivity and thermal shock stability for MgO partially stabilized zirconia. *Solid State Ionics* 40(41):750–753
108. Tretyakov JD, Muan A (1969) A new cell for electrochemical studies at elevated temperatures: design and properties of a cell involving a combination of Thorium oxide-Yttrium oxide and Zirconium oxide-Calcium oxide electrolytes. *J Electrochem Soc* 116:331–334
109. Swinkels DAJ (1970) Rapid determination of electronic conductivity limits of solid electrolytes. *J Electrochem Soc* 117:1267–1268
110. Huang K, Xia Y, Liu Q (1994) Rapid determination of electronic conductivity in MgO-partially stabilized ZrO_2 electrolytes using EMF method. *Solid State Ionics* 73:41–48
111. Steil MC, Thevenot F, Kleitz M (1997) Densification of yttria-stabilized zirconia impedance spectroscopy analysis. *J Electrochem Soc* 144:390–398
112. Nagata K, Goto KS (1983) New applications of oxygen sensors to ironmaking and steelmaking in Japan. *Solid State Ionics* 9(10):1249–1256
113. Janke D, Schwerdtfeger K (1979) A new immersion sensor for rapid electrochemical determination of dissolved oxygen in liquid metals. *Stahl Eisen* 99:825–829
114. Janke D, Schwerdtfeger K (1979) Test performance of the needle sensor for oxygen measurements under steelmaking conditions. *Stahl Eisen* 99:1211–1215
115. Janke D (1981) A new immersion sensor for the rapid electrochemical determination of dissolved oxygen in metallic melts. *Solid State Ionics* 3(4):599–604
116. Janke D (1983) Basic considerations on the design of oxygen probes for continuous measurements in steel melts. *Arch für das Eisenhüttenwes* 54:259–266
117. Janke D (1990) Recent developments of solid ionic sensors to control iron and steel bath composition. *Solid State Ionics* 40(41):764–769

118. Liu Q (1996) The development of high temperature electrochemical for metallurgical processes. *Solid State Ionics* 86–88:1037–1043
119. Janke D, Fischer WA (1976) Equilibria of chromium and manganese with oxygen in iron melts at 1600°C. *Arch für das Eisenhüttenwes* 47:147–151
120. Foulletier J (1982) Gas analysis with potentiometric sensors a review. *Sens Actuators* 3:295–314
121. Mochizuki M, Matsuoka M, Fujiwara R (1990) Improvement in response of commercialized oxygen sensor. *Solid State Ionics* 40(41):746–749
122. Worrell WL, Liu Q (1990) Development of an extended-life oxygen sensor for iron and steel melts. *Solid State Ionics* 40(41):761–763
123. Li F, Zhu Z, Li L (1994) A new way extending working-life of oxygen sensors in melt. *Solid State Ionics* 70(71):555–558
124. Jun Lou T, Hua Kong X, Qin Huang K, Guo Liu Q (2006) Solid reference electrode of metallurgical oxygen sensor. *J Iron Steel Res Int* 13:18–20
125. Ranganathan S, Janke D (1993) Thermodynamics of some new oxide reference materials for electrochemical oxygen sensors. *Scr Metall Mater* 29:305–310
126. Badwal SPS (1992) Zirconia-based solid electrolytes: microstructure, stability and ionic conductivity. *Solid State Ionics* 52:23–32
127. Inaba H, Tagawa H (1996) Ceria-based solid electrolytes. *Solid State Ionics* 83:1–16
128. Geller RF (1934) Yavorsky PJ (1945) Effects of some oxide additions on the thermal length changes of zirconia. *J Res Natl Bur Stand* 35:87–110
129. Guo X, Maier J (2009) Ionically conducting two-dimensional heterostructures. *Adv Mater* 21:2619–2631
130. Fabbri E, Pergolesi D, Traversa E (2010) Ionic conductivity in oxide heterostructures: the role of interfaces. *Sci Technol Adv Mater* 11:1–9
131. Otsuka K, Matsunaga K, Nakamura A et al (2004) Effects of dislocations on the oxygen ionic conduction in yttria stabilized zirconia. *Mater Trans* 45:2042–2047
132. Wilhelm RV, Howarth DS (1979) Iron oxide-doped yttria-stabilized zirconia ceramic: iron solubility and electrical conductivity. *Am Ceram Soc Bull* 58:228–232
133. Hartmanova M, Machovic L, Koller A et al (1984) Electrical conductivity and structure of CaO-stabilized zirconia doped with copper and iron. *Solid State Ionics* 14:93–105
134. Boukamp BA, Raming TP, Winnubst AJA, Verweij H (2003) Electrochemical characterisation of 3Y-TZP-Fe₂O₃ composites. *Solid State Ionics* 158:381–394
135. Chastanat M, Gateller C, Jon M, Olette M (1973) The rapid determination of oxygen activity in molten steel by means of a solid electrolyte probe with a solid state reference. European Coal and Steel Community Commission
136. Liu Q, An S, Qiu W (1999) Study on thermal expansion and thermal shock resistance of MgO-PSZ. *Solid State Ionics* 121:61–65
137. An S, Wu X, Wu W, Liu Q (1992) Effect of heat treatment on structure and properties of MgO-PSZ electrolyte. *Solid State Ionics* 57:31–34